

# Visible-light-driven removal of atrazine by durable hollow core-shell $\text{TiO}_2@\text{LaFeO}_3$ heterojunction coupling with peroxyomonosulfate via enhanced electron-transfer

Kexin Wei <sup>a,b</sup>, Andac Armutlulu <sup>c</sup>, Yinxu Wang <sup>a</sup>, Gang Yao <sup>b,d</sup>, Ruzhen Xie <sup>a,\*</sup>, Bo Lai <sup>a,b,\*\*</sup>

<sup>a</sup> State Key Laboratory of Hydraulics and Mountain River Engineering, College of Architecture and Environment, Sichuan University, Chengdu 610065, China

<sup>b</sup> Sino-German Centre for Water and Health Research, Sichuan University, Chengdu 610065, China

<sup>c</sup> Department of Mechanical and Process Engineering, ETH Zürich, Leonhardstrasse 27, 8092 Zurich, Switzerland

<sup>d</sup> Institute of Environmental Engineering, RWTH Aachen University, Germany



## ARTICLE INFO

### Keywords:

Perovskite

Photocatalyst

Reactive oxidation species

PMS, AOPs

## ABSTRACT

Insufficient charge-carriers separation and deteriorated recycling are still bottlenecks limiting practical photocatalytic water purification. Herein, we developed a durable hollow core-shell  $\text{TiO}_2@\text{LaFeO}_3$  (TLFO) nanosphere via facile carbon-sphere-templated method and sol-gel process, and applied it as heterojunction photocatalyst coupled with peroxyomonosulfate (PMS) for efficient atrazine (ATZ) removal via enhanced electron-transfer. The built-in electric field originated from the three-dimensional heterojunction between  $\text{TiO}_2$  and  $\text{LaFeO}_3$ , acting as charge transfer driving force, enhanced the charge separation rate. Meanwhile, PMS could function as electron acceptor to boost photogenerated charge separation and maximize reactive oxidant species (e.g.,  $\cdot\text{OH}$ ,  $\text{SO}_4^{\cdot-}$ ,  $\text{O}_2^{\cdot-}$  and  ${}^1\text{O}_2$ ) production. Therefore, the fabricated TLFO heterojunction exhibited outstanding reusability, and superior ATZ removal efficiency without detectable metal ion leaching. This work successfully demonstrates the synergistic effect and superior hollow structure of TLFO heterojunction with promoted light utilization and PMS activation, which offers potential application for efficient abating environmental pollution using solar energy.

## 1. Introduction

The synthetic s-triazine herbicides are commonly used in agricultural and industrial areas and have heavily contaminated the natural environment due to their low biodegradability, high persistence and mobility as well as extensive usage all over the world [1,2]. Among these herbicides, atrazine (2-chloro-4-ethylamino-6-isopropylamino-s-triazine, ATZ) is one of the most widely used and frequently detected pollutants in the aquatic environment. According to previous studies, ATZ is detrimental to aquatic and terrestrial organisms even at low concentrations of about 60 ng/L, and has been determined as endocrine disrupting chemical and potential carcinogen [3,4]. However, conventional technologies such as biological treatment, adsorption, sedimentation, and coagulation can hardly achieve high ATZ removal efficiency [5]. Consequently, the search for a reliable technology to eliminate persistent pollutant ATZ efficiently is of great importance, so as to

alleviate its serious adverse effects on water environment.

Advanced oxidation processes (AOPs) exhibit high efficiency in abating organic pollutants ATZ, such as photocatalysis [6], Fenton oxidation [7], persulfate activation [8], electrochemical oxidation [9], etc. Among these oxidation processes, heterogeneous photocatalysis provides a promising avenue for utilizing solar light as renewable energy source to initiate chemical transformation and pollutant degradation [10]. However, simple photocatalysis system has its limitations in terms of moderate oxidation capacity and environmental susceptibility. Peroxyomonosulfate (PMS)-assisted photocatalysis has drawn much attention for organic pollutant mineralization due to its excellent oxidation capability, improved energy utilization, wide adaptability, and enormous economic and environmental benefits [11,12]. Previous studies have shown that PMS could function dually as sulfate radical ( $\text{SO}_4^{\cdot-}$ ) precursor through one-electron reduction as well as electron acceptor to impede photogenerated charge recombination [13–15]. With the help of

\* Corresponding author.

\*\* Corresponding author at: State Key Laboratory of Hydraulics and Mountain River Engineering, College of Architecture and Environment, Sichuan University, Chengdu 610065, China.

E-mail addresses: [xieruzhen@scu.edu.cn](mailto:xieruzhen@scu.edu.cn) (R. Xie), [laibo@scu.edu.cn](mailto:laibo@scu.edu.cn) (B. Lai).

PMS, the photogenerated electrons are consumed for  $\text{SO}_4^{\bullet-}$  generation, leaving more photogenerated holes ( $\text{h}^+$ ) for enhanced hydroxyl radical ( $\cdot\text{OH}$ ) generation. The generated  $\text{SO}_4^{\bullet-}$  has higher redox potentials (2.5–3.1 V) and extended half-life (30–40  $\mu\text{s}$ ) as compared to  $\cdot\text{OH}$  (1.8–2.7 V, < 1  $\mu\text{s}$ ) [16–18]. Therefore, introducing PMS into photocatalytic process offers an efficient solution to boost photogenerated  $e^-$ - $\text{h}^+$  pairs separation efficiency through capturing electrons, which leads to stronger oxidation capability for organic pollutants destruction and endows this technology to be one of the most effective technologies for pollutant decontamination.

The key factor of PMS-assisted photocatalysis for refractory organic pollutants degradation lies in the physicochemical properties of heterogeneous photocatalysts, such as wide spectral response, charge separation rate, PMS activation capability and stability [19]. Traditional titanium oxide ( $\text{TiO}_2$ ) has been widely studied as photocatalyst for environmental disinfection and energy conversion owing to its photo-stability, strong oxidation capability and non-toxic nature. However, the practical photocatalytic applications of  $\text{TiO}_2$  is limited by its large bandgap value that can hardly be excited by visible light. Thus, visible-light-sensitive photocatalyst is of great significance to address the concerns arising from the bottleneck of the poor visible light utilization [20]. Lanthanum ferrite ( $\text{LaFeO}_3$ ), a member of the group of perovskite with narrow bandgap value (2.0–2.7 eV), is a promising visible-light-driven heterogeneous photocatalyst with advantages of good chemical stability and photocatalytic activity originated from its unique electronic and crystal structure [21]. Specifically,  $\text{LaFeO}_3$  (LFO) exhibits excellent optical absorption ability and visible light utilization efficiency due to its intrinsic narrow bandgap structure, which could be easily activated by visible light and generate charge carriers as well as reactive oxygen species (ROS) to accelerate pollutant degradation. Furthermore, the redox cycle of Fe on the surface of LFO could act as reaction site and initiate  $\text{SO}_4^{\bullet-}$  and  $\cdot\text{OH}$  formation during PMS-assisted photocatalytic process. Simultaneously, the consumed Fe(II) could be regenerated via photo-assisted reduction of Fe(III) [22]. However, since Fe ions of LFO provide active sites for PMS activation, the limitations of deteriorated reactivity and secondary pollution caused by metal leaching remain inevitable. In addition, the CB position of LFO usually locates at 0.2 eV vs. NHE, which renders it difficult to induce the reduction of  $\text{O}_2$  to  $\text{O}_2^{\bullet-}$  under visible light ( $\text{O}_2/\text{O}_2^{\bullet-} = -0.33$  eV vs. NHE) [23]. Moreover, sole LFO bulks suffer from agglomeration and rapid charge recombination, which competes with useful extraction of charge carriers and results in energy loss and photoreactivity deterioration [24,25]. To realize effective photocatalysis, the properties of LFO have been easily regulated by A/B site substitution, heterojunction fabrication or morphology controlling, so as to induce lattice defects, enhance visible light response and boost electron transfer process [26]. With this in mind, constructing heterojunction would be an effective method to accelerate charge separation in LFO with enhanced quantum efficiency to optimize PMS assisted photocatalytic performance. In previous studies, LFO was integrated with various semiconductors to obtain heterojunctions such as  $\text{LaFeO}_3/\text{g-C}_3\text{N}_4$  [27],  $\text{LaFeO}_3/\text{TiO}_2$  [28], and  $\text{LaFeO}_3/\text{g-C}_3\text{N}_4/\text{BiFeO}_3$  [29], which constructed multiphase components and highly suppressed the recombination of charge carriers via the intimate contact interface. The formed heterojunction endowed efficient charge-carrier extraction and utilization due to the internal electric field at the interface, which hindered the recombination of electron-hole pairs and contribute to enhanced pollutants removal [27]. In particular, a heterojunction morphology with hollow core-shell structure has attracted increasing attention, due to their improved mass transfer and charge separation efficiency, three-dimensional heterostructure, enlarged surface area and enhanced light utilization, as compared to their bulk counterparts of the same weight [30]. Wang et al. [31] developed  $\text{MoSe}_2@\text{Bi}_2\text{S}_3/\text{CdS}$  hollow core-shell photocatalyst as ternary Z-Scheme heterojunction for TCP degradation and  $\text{H}_2$  generation. The hollow nanostructure showed improved full spectrum absorption and optimized energy band with higher electronic hybridization degree,

which realized improvement of light utilization and provided multi-channels for efficient charge separation. Besides, hollow core-shell  $\text{TiO}_2@\text{Fe-MOFs}$  nanotube was developed with enhanced photoelectrocatalytic characteristics for phenol degradation. The internal electric field across the three-dimensional heterojunction highly suppressed the recombination of charge carriers, which contributed to enhanced phenol decontamination via  $\text{O}_2^{\bullet-}$ ,  $\cdot\text{OH}$  and  $\text{h}^+$  generation [32]. Thus, it is reasonable to speculate that combining LFO with other semiconductors to fabricate hollow core-shell heterojunction would benefit from the internal electric field originated from the interfacial contact. In addition, the hierarchical photocatalyst would be feasible to realize direct charge transfer with PMS for efficient organic degradation, without losing active species and metal leaching during the cycle reactions. Such stability and eco-friendliness are highly desirable in the PMS-assisted photocatalysis process for practical application.

Therefore, in this work, we developed a hollow core-shell  $\text{TiO}_2@-\text{LaFeO}_3$  (TLFO) via a template-based strategy coupled with sol-gel method for PMS-assisted degradation of typical pesticide pollutant ATZ under visible light irradiation. The three-dimensional heterojunction between the stable  $\text{TiO}_2$  and visible-light-sensitive  $\text{LaFeO}_3$  can efficiently improve photoreactivity without metal leaching and deterioration. The enhanced separation and transfer capability of photogenerated charge carriers within TLFO were evaluated by photoluminescence (PL) spectroscopy, transient photocurrent (i-t), electrochemical impedance spectroscopy (EIS) and Mott-Schottky (MS) analysis. Moreover, the structure and photocatalytic performance of the photocatalysts were investigated. The improved electron transfer mechanism underlying ATZ removal by PMS-assisted TLFO heterojunction photocatalysis was discussed in detail. Finally, the possible ATZ removal pathway was explored via identifying intermediates and products with liquid chromatography/mass spectrometry (LC/MS).

## 2. Experimental

### 2.1. Chemical reagents

The details of chemicals used are listed in [Test S1](#).

### 2.2. Catalyst preparation

#### 2.2.1. Synthesis of carbon nanospheres

Carbon nanospheres were fabricated through a hydrothermal carbonization method. 8 g glucose was dissolved in 40 mL distilled water to form a clear solution and was used as starting material to prepare carbon spheres. The solution was transferred into a 50 mL Teflon-lined autoclave, sealed and maintained at 170 °C for 10 h. The resulting dark brown products were separated by centrifugation and washed with distilled water and ethanol for several times, respectively, until the solution turned clear. Finally, carbon nanospheres in the form of powder were obtained upon drying in an oven at 80 °C in ambient air.

#### 2.2.2. Synthesis of C-doped hollow $\text{TiO}_2$ nanospheres

Hollow  $\text{TiO}_2$  was synthesized by a sol-gel method using carbon sphere as template. 100 mg as-obtained carbon nanospheres were dispersed into 100 mL absolute ethanol under sonication for 30 min. The suspension was continuously stirred for 1 h, and 9 mL TBOT was introduced dropwise under magnetic agitation. Subsequently, a solution of EtOH:  $\text{H}_2\text{O}$  with a ratio of 5:1 was introduced dropwise under vigorous stirring for 3 h at a temperature of  $60 \pm 1$  °C, allowing adsorption and hydrolysis of TBOT on the surface of carbon spheres. Following the aging, the precursor underwent suction filtration, and the filter cake was dried in an oven at 80 °C to form C@ $\text{TiO}_2$  nanosphere. Finally, the powder was subjected to calcination process at 600 °C for 3 h to remove carbon sphere and obtain hollow  $\text{TiO}_2$  nanosphere, which is denoted as h- $\text{TiO}_2$ . For comparison, solid  $\text{TiO}_2$  nanospheres were synthesized as a control group via the same procedure in the absence of

carbon sphere templates and denoted as solid  $\text{TiO}_2$ .

### 2.2.3. Synthesis of hollow $\text{TiO}_2@\text{LFO}$ core-shell nanospheres

The hollow core-shell  $\text{TiO}_2@\text{LFO}$  was fabricated through in-situ sol-gel deposition method. Stoichiometric amounts of  $\text{La}(\text{NO}_3)_3 \cdot 6\text{H}_2\text{O}$ ,  $\text{Fe}(\text{NO}_3)_3 \cdot 6\text{H}_2\text{O}$  and citric acid (molar ratio of La:Fe = 1:1) were dissolved in 50 mL distilled water to yield a homogeneous brownish yellow solution. After continuous stirring for 2 h, ammonia was added to the solution dropwise until pH value reached about 7.5, which is then followed by the addition of 3 mL ethylene glycol as chelating agent. 600 mg as-obtained h- $\text{TiO}_2$  was dispersed into the above solution and sonicated for 30 min to achieve a uniform coating of LFO precursor on h- $\text{TiO}_2$ . The mixture suspension was stirred and heated to 90 °C until it became a gel. Subsequently, the suspension underwent suction filtration, whereby the product collected was subjected to the drying process at 105 °C and calcination process at 600 °C for 4 h to ensure good crystallinity and adhesion of the LFO coating, resulting in hollow core-shell  $\text{TiO}_2@\text{LFO}$ . The synthesis of TLFO core-shell hollow composite is illustrated in Fig. 1.

### 2.3. Experimental procedure

The photocatalytic activity was evaluated by the degradation of ATZ via activating PMS under visible light irradiation (LED lamp, 200 W, 410–760 nm, CEL-LAB200E7, Beijing China Education Au-light). All the experiments were performed in 100 mL quartz tubes containing 50 mL ATZ solution. The temperature was controlled at  $30 \pm 1$  °C by the circulating cooling water, and the pH of the solution was not adjusted unless otherwise stated. Typically, the required amount of TLFO was added firstly to the ATZ solution (2.5 mg/L) in the dark under continuous magnetic stirring, and appropriate concentration of PMS was then added to the solution to initiate the reaction under visible light irradiation. Meanwhile, magnetic stirring was kept at a constant speed throughout the reaction. Periodically, 1 mL sample was withdrawn and filtered through 0.45 μm PTFE syringe filter for further analysis.

Radical quenching experiments were performed with TBA, EtOH, BQ, EDTA-2Na and FFA to determine the active radicals generated in the reaction. All experiments were performed for three times, and the mean value of the data was presented.

### 2.4. Analytic methods

The crystal phase of TLFO was detected by X-ray diffractometer (XRD, PANalytical B.V., Holland) with  $\text{Cu K}\alpha$  radiation. Surface elements and valence states of TLFO were analyzed by X-ray photoelectron spectrometer (XPS, AXIS Ultra DLD, Kratos Co). The surface morphology of the photocatalysts during synthesis process including carbon sphere templates, hollow  $\text{TiO}_2$  and as-prepared TLFO were observed by scanning electron microscope (SEM, SU-8010, Hitachi) and transmission electron microscope (TEM, FEI Talos F200x, FEI Company, USA). The elemental composition and distribution were detected with elemental mapping in a Super-XTM system. The zeta potential and size distribution were analyzed on particle sizing systems (PSS, Santa Barbara, CA, USA). The ultraviolet-visible diffuse reflectance spectrum (UV-Vis DRS) of different photocatalysts were measured using a UV-Vis spectrophotometer equipped with an integration sphere (UV8000, Yuanxi, China).

Photoelectrochemical measurements including electrochemical impedance spectroscopy (EIS), transient photocurrent (i-t) and Mott-Schottky plot (M-S) were conducted with an electrochemical station (CHI760E, Chenhua Instrument, shanghai, China). Photoluminescence (PL) spectrum was conducted with the Edinburgh FLS 1000 fluorescence spectrophotometer.

The concentration of ATZ during photodegradation was analyzed with a high-performance liquid chromatography system (HPLC, Agilent 1260, USA) equipped with an Eclipse XDB C-18 (5 μm, 4.6 × 250 mm) column (Test S2). The intermediates and products of ATZ degradation were analyzed by liquid chromatograph coupled with a mass spectrometry (LC/MS, TSQ Quantum Ultra, (Thermo Fisher Scientific, America)) equipped with C-18 column (5.0 μm, 2.1 × 150 mm) (Test S3). Total organic carbon (TOC) of the ATZ solution was analyzed via TOC analyzer (Shimazu, Japan). The concentration of iron leaching was quantified by atomic adsorption with graphite furnace (AA6880, SHIMADZU). Consumed PMS concentration during degradation was analyzed via the ABTS method using a UV-Vis spectrophotometer (UV1800, SHIMADZU). ROS were detected by electron paramagnetic resonance (EPR) on Bruker EMX plus X-band CW EPR spectrometer (microwave frequency, 9.83 GHz; microwave power, 2.00 mW). In addition, pH value of the solution was adjusted with  $\text{H}_2\text{SO}_4$  (0.1 M) and NaOH (0.1 M) and detected via Rex pH meter (model PHS-3C).

The removal efficiency of different systems was fitted by the pseudo-first-order kinetic model. The kinetic rate constant can be calculated as (Eq. (1)).

$$\ln([ATZ]/[ATZ]_0) = -k_{obs} \cdot t \quad (1)$$

Where  $[ATZ]_0$  and  $[ATZ]$  (mg/L) represent the initial ATZ concentration and concentration at sampling point time, while  $k_{obs}$  ( $\text{min}^{-1}$ ) represents the pseudo-first-order rate constants and  $t$  (min) stands for the reaction time.

## 3. Results and discussion

### 3.1. Characterization of TLFO

#### 3.1.1. Morphology and chemical structures

The crystal structure of TLFO is determined by XRD, and the results are demonstrated in Fig. 2. Diffraction peaks at 25.1 °, 37.9 °, 48.0 °, 53.6 °, 55.0 ° and 62.6 ° are assigned to the (101), (004), (200), (105), (211) and (204) planes of typical anatase  $\text{TiO}_2$  (JCPDS No.21-1272). Trace amount of rutile  $\text{TiO}_2$  (JCPDS No.21-1276) can be observed on hollow  $\text{TiO}_2$  spheres, which could be attributed to the formation of anatase to rutile at annealing temperature of 500–600 °C [33]. The co-existence of anatase and rutile results in phase-heterojunction, facilitating the separation of photogenerated carriers across the interface and enhancing the photocatalytic activity [34]. Furthermore, both  $\text{TiO}_2$  and orthorhombic phase LFO (JCPDS No.37-1493) at diffraction peaks of 32.2 °, 46.1 °, and 57.4 ° corresponding to the respective (110), (200), and (210) planes can be observed in TLFO, indicating successful construction of the binary heterojunction of  $\text{TiO}_2$  and LFO on TLFO [24].

The morphologies of the photocatalyst during synthesis are presented in Fig. 3. It reveals in Fig. 3a that the carbon templates featuring an average diameter of 500 nm have rather uniform size distribution

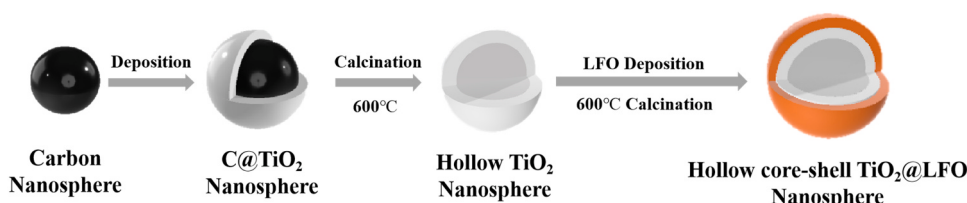
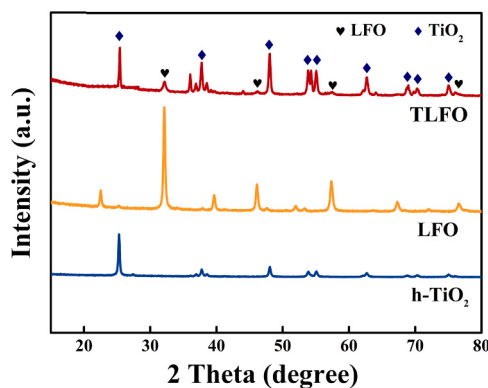


Fig. 1. Schematic illustration of the synthesis process of hollow core-shell  $\text{TiO}_2@\text{LFO}$ .



**Fig. 2.** The XRD patterns of h-TiO<sub>2</sub>, LFO and TLFO samples.

and good integrity, which is beneficial for the growth of TiO<sub>2</sub> layer. In Fig. 3b, the h-TiO<sub>2</sub> shell appears as an interconnected framework with a certain degree of shrinkage in size, which might be attributed to the CO<sub>2</sub> release during calcination [20]. With the deposition of LFO, TLFO nanospheres with diameter of about 450 nm were obtained, as shown in Fig. 3c,d). The particle size is in consistence with the size distribution analysis (Fig. S1), suggesting that the dominating diameter of TLFO nanoparticles is about 450 nm. The elemental mapping of TLFO demonstrates that La, Fe, Ti, C and O are homogeneously distributed on the surface of TLFO (Fig. 3g–l). Specifically, La and Fe elements are ascribed to LFO shell layer while Ti can be attributed to the hollow TiO<sub>2</sub>.

TEM images of both fresh and recycled TLFO further reveal the hollow core-shell structure of the nanospheres. As presented in Fig. 3(d, e), TLFO demonstrates an average diameter of 450 nm and a shell thickness of about 80 nm. Furthermore, recycled TLFO shows stable hollow structure after six cycles. Additionally, some broken spheres are also observed with pores on the surface of the photocatalyst, which might facilitate the utilization of light as well as the permeation of substrates during the photodegradation. The heterojunction formed between the hollow TiO<sub>2</sub> spheres and LFO shell was in the form of three-dimensional interfacial contact, favoring the photocatalysis and electron transfer process. In addition, HRTEM image of fresh TLFO in Fig. 3e shows the lattice fringe spacings of 0.35 nm and 0.28 nm corresponding to the (101) plane of anatase TiO<sub>2</sub> and (110) plane of orthorhombic LFO, respectively [28,35]. In general, SEM and TEM studies confirm the successful preparation of the hollow core-shell geometry of TLFO nanospheres, which enable good structural and photocatalytic properties in ATZ degradation.

XPS analysis is employed to further investigate the composition and oxidation states of elements in TLFO. According to full-scanned XPS spectrum (Fig. 4a), the presence of La, Fe, Ti, C, O is confirmed in the TLFO heterojunction, which is in agreement with the elemental mapping analysis. Fig. 4b presents the high-resolution spectra of La 3d, where the peaks centered at 834.7 eV and 851.4 eV are ascribed to La 3d<sub>5/2</sub>, while 838.4 eV and 855.3 eV are assigned La 3d<sub>3/2</sub>. The separation between two peaks is around 16.8 eV and indicates the existence of La(III) in TLFO [36]. The XPS spectrum reveals peaks of Fe 2p located at binding energy near 710.0 eV, 718.9 eV and 724 eV, which are attributed to Fe

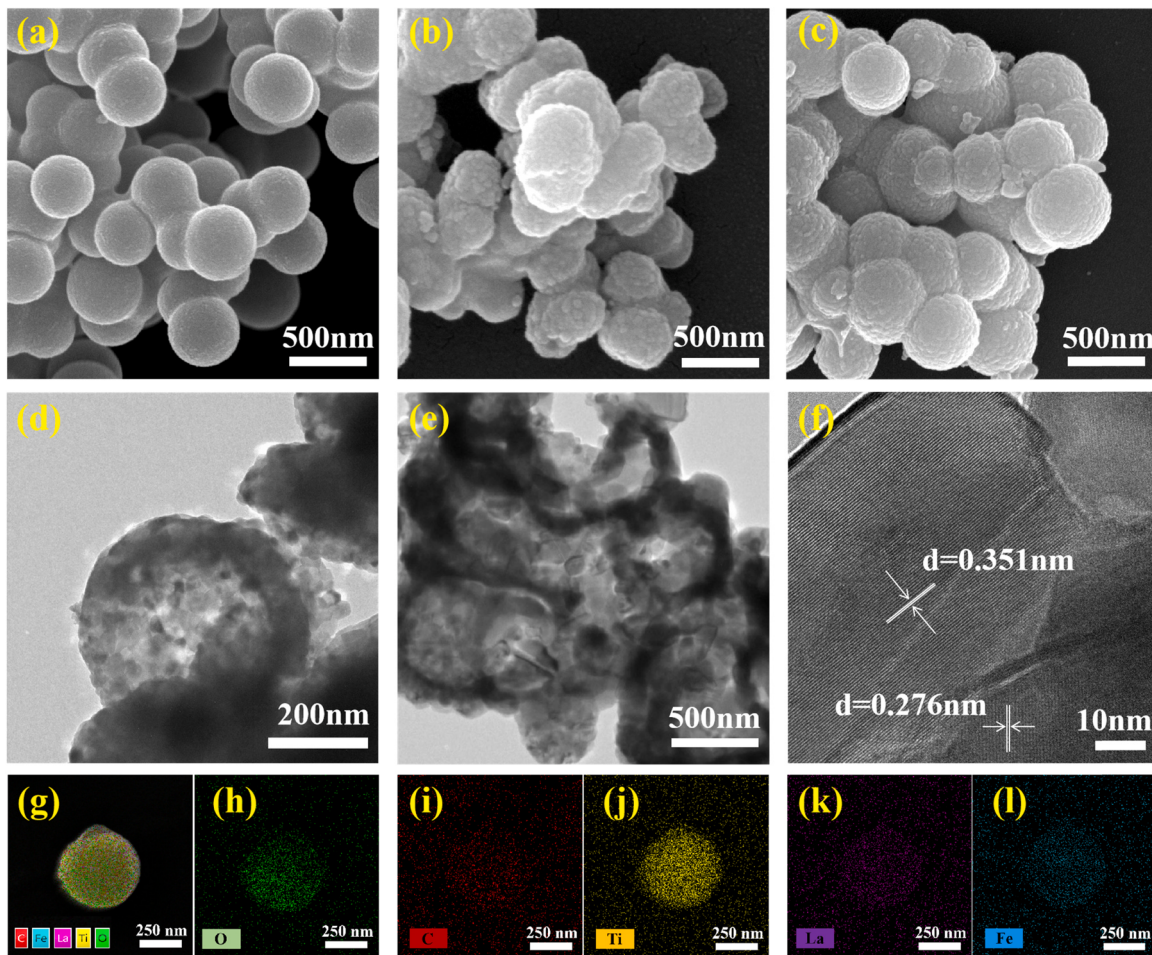


**Fig. 3.** The SEM images of (a) carbon spheres, (b) h-TiO<sub>2</sub>, (c) TLFO, and TEM images of (d) fresh TLFO, (e) recycled TLFO after 6 times, (f) HRTEM images of fresh TLFO, and (g–l) the elemental mappings of fresh TLFO.

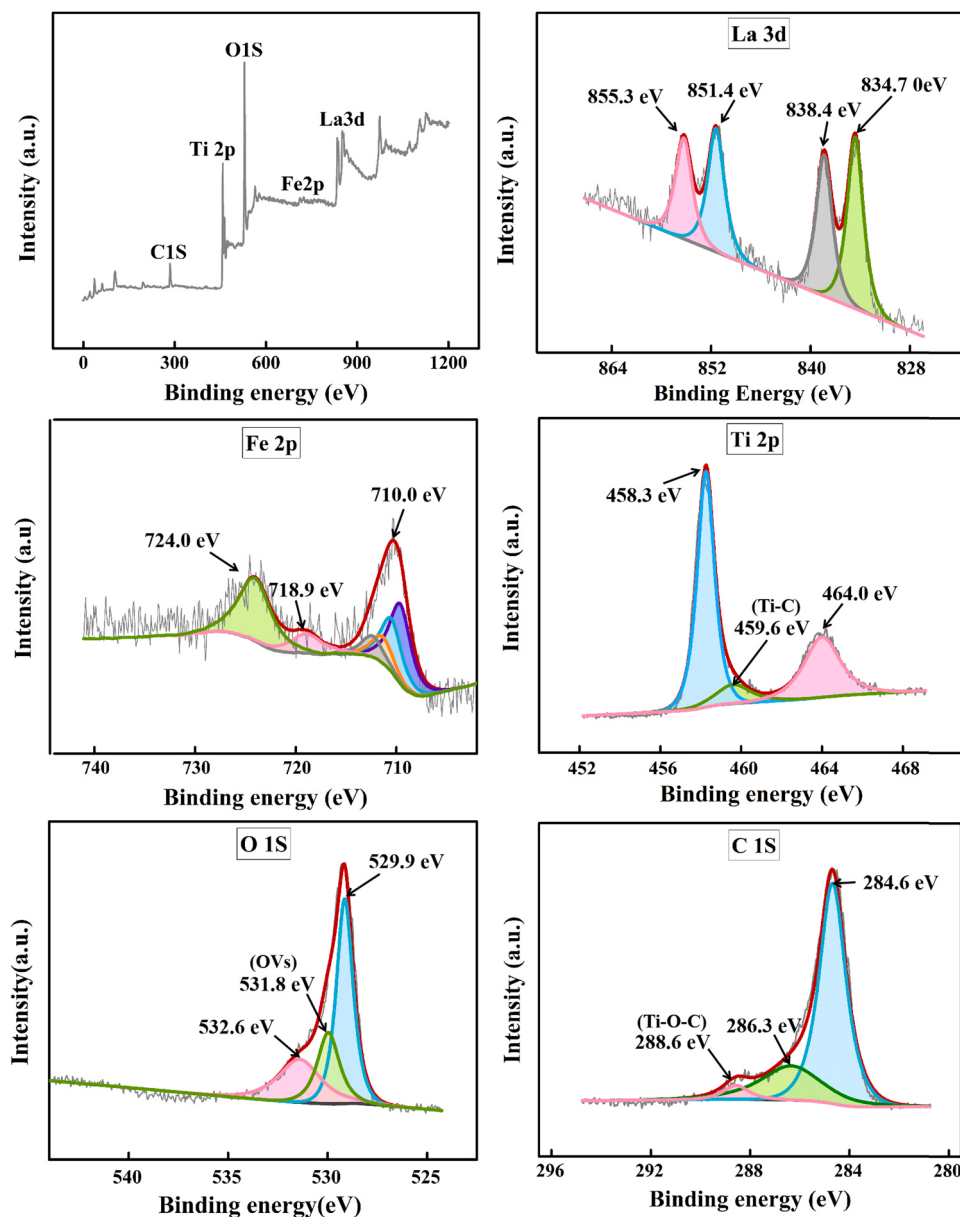


**Fig. 4.** XPS spectra of TLFO particles: (a) full-range scan, (b) La 3d core level, (c) Fe 2p core level, (d) Ti 2p core level, (e) O 1s core level, and (f) C 1s core level.

2p<sub>3/2</sub>, shake-up satellite and Fe 2p<sub>1/2</sub>, respectively (Fig. 4c). The divided peaks at 709.9 eV and 723.7 eV are characteristic of Fe(II), whereas the peaks located at 712.0 eV and 726.0 eV are assigned to Fe(III) ions, suggesting the mixed oxidation states of both Fe(II) and Fe(III) exist in TLFO [7,37]. The peaks shown in Fig. 4d at binding energies of 458.3 eV and 464.0 eV are attributed to Ti 2p<sub>3/2</sub> and Ti 2p<sub>1/2</sub> in hollow TiO<sub>2</sub>, respectively. The spin-orbit splitting of Ti 2p is 5.7 eV, indicating the presence of Ti(IV) oxidation state in TLFO [38]. Besides, the peak located at 459.6 eV can be ascribed to the Ti-C bonds on TiO<sub>2</sub>, suggesting carbon doped into the lattice of TiO<sub>2</sub> while using carbon nanosphere as synthetic templates [13].

The O 1s XPS spectrum (Fig. 4e) consists of three peaks at binding energies of 529.9 eV, 531.8 eV and 532.6 eV, corresponding to lattice oxygen, adsorbed oxygen and oxygen within hydroxyl groups from adsorbed water molecules, respectively [39]. Among them, the adsorbed oxygen at 531.8 eV in TLFO photocatalyst corresponds to oxygen vacancies due to its general existence on surface oxygen defects, confirming the presence of the oxygen vacancies in the as-prepared TLFO [40]. In addition, the C 1s XPS spectra in Fig. 4f could be fitted into three

major peaks located at 284.6 eV, 286.3 eV and 288.6 eV. The peak observed at 288.6 eV is characteristic of Ti-O-C, suggesting amorphous carbon doping into the TiO<sub>2</sub> lattice [41]. This bond structure could not only facilitate the charge transfer and improve photocatalytic activity, but also helps to broaden light absorption via narrowing bandgap value, which is further demonstrated by the UV-Vis DRS results.

### 3.1.2. Optical and photoelectrochemical properties

The optical properties of the prepared samples were measured using UV-Vis DRS. As demonstrated in Fig. 5a, LFO exhibits strong photoabsorption in the wavelength range of 320–600 nm. The maximum light absorption for pure TiO<sub>2</sub> is observed in the UV region at around 340 nm, and the absorption band edge locates at about 395 nm. The adsorption edge of h-TiO<sub>2</sub> red shifts to the visible light region at around 410 nm, indicating higher visible light absorption compared to pure TiO<sub>2</sub> due to its unique structure and doped carbon during synthesis. Upon introducing visible-light-sensitive LFO, the binary heterojunction of both solid TiO<sub>2</sub>@LFO and TLFO exhibit an obviously enhanced visible irradiation response. In particular, the deposited LFO shell on the

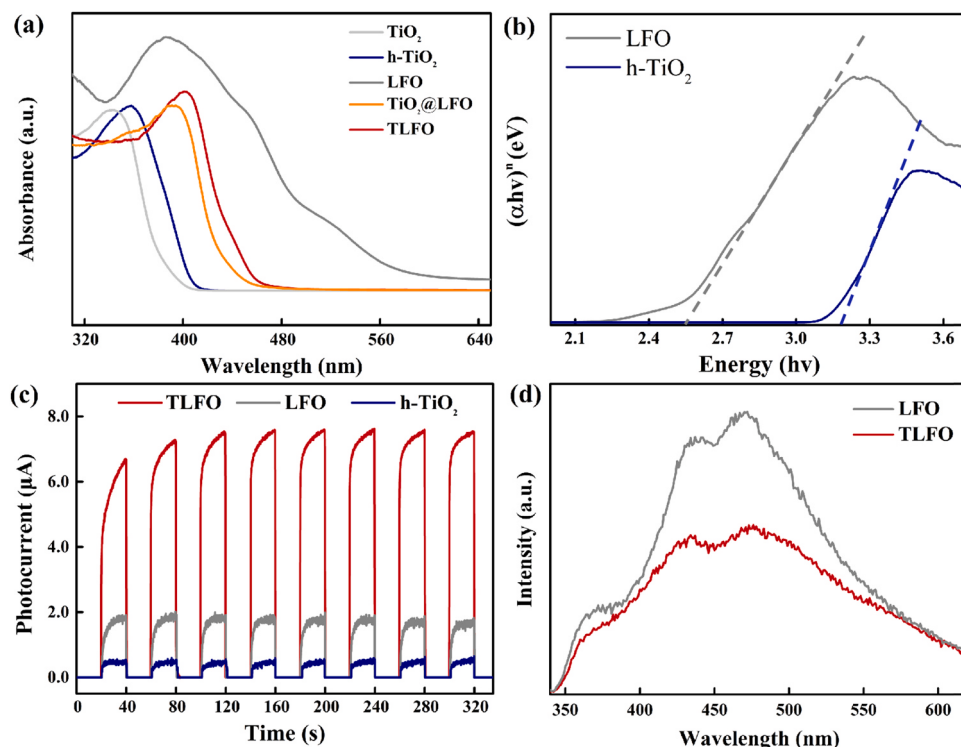


**Fig. 5.** Photoelectrical properties of different photocatalysts: (a) UV-Vis DRS, (b) Tauc plots, (c) transient photocurrent, and (d) PL measurement.

surface of h-TiO<sub>2</sub> successfully extends adsorption edge of TLFO to 450 nm, which could be attributed to higher visible-light utilization efficiency and multiple reflection of incident light within hollow TLFO. Moreover, the bandgap energy is evaluated using Tauc equation by extrapolating the linear fitted regions to  $(\alpha h\nu)^n = 0$  (Test S4). The Tauc plots (Fig. 5b) demonstrate the bandgap locate at 2.56 eV and 3.16 eV for LFO and h-TiO<sub>2</sub>, respectively. Compounding h-TiO<sub>2</sub> core with LFO shell resulted TLFO with different adsorption edge, indicating electrostatic interaction existed between h-TiO<sub>2</sub> and LFO during hybridization, which could increase the light-harvesting capability of TLFO as compared to h-TiO<sub>2</sub> and make TLFO perform better as a visible-light-driven photocatalyst.

The separation and transfer of photogenerated charge carriers were investigated by photoelectrochemical test. As shown in Fig. 5c, the transient photocurrent response of pure LFO, single h-TiO<sub>2</sub> and TLFO under dark and visible light were investigated for several light on-off cycles. TLFO heterojunction exhibits remarkably stronger visible-light-driven photocurrent (7.63 μA) under irradiation, which is more than 3-fold and 11-fold of LFO (2.01 μA) and h-TiO<sub>2</sub> (0.65 μA), respectively. This outstanding photocurrent response of TLFO might be attributed to the three-dimensional charge transfer path provided by the hollow core-shell heterostructure, resulting in efficient electron migration and extended lifetime of photogenerated carriers [42]. In addition, EIS measurement was conducted to evaluate the interfacial properties and charge transfer resistance of the photocatalysts. The Nyquist arc radius of TLFO heterojunction is smaller than that of LFO and h-TiO<sub>2</sub> (Fig. S2), suggesting that LFO coating on the surface of h-TiO<sub>2</sub> facilitates the electron mobility owing to the broader platform and formed heterojunction within the hollow TLFO [43]. Besides, Fig. 5d shows the PL spectra of the pure LFO and TLFO at an excitation wavelength of 320 nm. It is known that pure LFO is vulnerable to rapid charge recombination and resulting energy loss during photocatalysis, leading to extremely short lifetime of photogenerated carriers [19]. The weak intensity of PL emission of TLFO represents a suppressed recombination of charge carriers with prolonged lifetime when integrating LFO with h-TiO<sub>2</sub>. All these analysis results demonstrate that the hollow core-shell

TLFO heterojunction exhibits superior light-harvesting capability and excellent electron transfer efficiency, which extends the utilization of photogenerated charge carriers and further promotes ROS generation in the PMS-assisted photocatalysis process.

### 3.2. Photocatalytic degradation of ATZ under different conditions

The ATZ photocatalytic degradation performance in different systems was investigated, including different conditions of sole visible light, PMS, TLFO, Vis/PMS, Vis/TLFO, TLFO/PMS, Vis/TLFO/PMS. It can be observed from Fig. 6a, ATZ degradation rate in the systems of sole visible light, PMS and TLFO were all less than 5%, indicating the absorption of ATZ on TLFO and the direct oxidation of ATZ by visible light or PMS were weak and negligible (Fig. S3). Meanwhile, the removal of ATZ in the Vis/PMS and Vis/TLFO systems were also insignificant, which were only about 5% and 6%, respectively. The removal of ATZ in TLFO/PMS system without visible light irradiation was 14% within 120 min, suggesting the active sites such as Fe(II)/Fe(III) redox pair on TLFO could contribute to PMS heterogeneous activation and generate SO<sub>4</sub><sup>•-</sup> for ATZ removal. However, the electron transfer between TLFO and PMS might be inefficient [44]. Complete ATZ removal was observed in the system of Vis/TLFO/PMS within 90 min, indicating the superior synergistic effect between PMS activation and TLFO photocatalyst under visible light illumination. The pseudo first-order kinetic model was performed to further determine the degradation efficiency in different systems. The pseudo-first-order rate constant k<sub>obs</sub> of the Vis/TLFO/PMS system ( $2.96 \times 10^{-2} \text{ min}^{-1}$ ) was found to be about 16.7, 34.4 and 72.3 times higher than that of the TLFO/PMS ( $1.77 \times 10^{-3} \text{ min}^{-1}$ ), Vis/TLFO ( $8.61 \times 10^{-4} \text{ min}^{-1}$ ) and Vis/PMS ( $4.09 \times 10^{-4} \text{ min}^{-1}$ ) systems (Fig. S4), respectively. Furthermore, the TOC removal (37.04%) of the Vis/PMS/TLFO system was evaluated to be higher than those of other systems, which was 10.4, 15.6 and 16.8 times higher than that of the TLFO/PMS (3.56%), Vis/TLFO (2.37%), and Vis/PMS (2.04%) systems (Fig. S5), respectively. These results further confirmed the synergistic effect of Vis/PMS/TLFO system and the excellent photocatalytic capability of TLFO with the assistance of PMS.

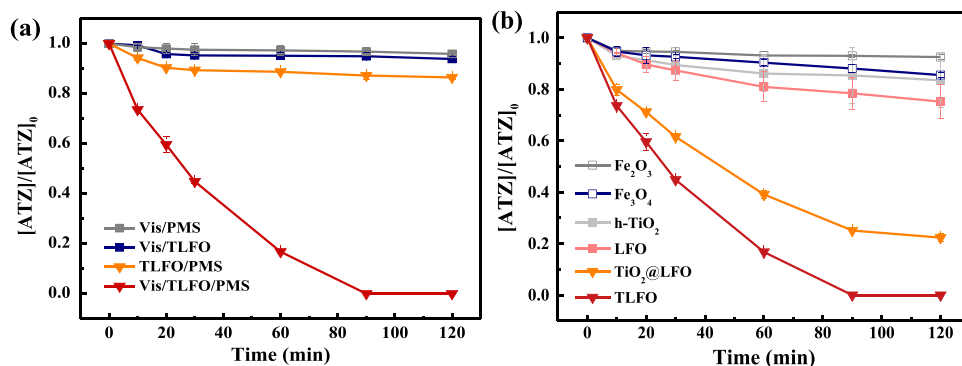


**Fig. 6.** (a) Performance of ATZ photodegradation in different systems, and (b) performance of ATZ photodegradation of different materials. (Conditions:  $[ATZ]_0 = 2.5 \text{ mg/L}$ ,  $[\text{photocatalyst}]_0 = 0.4 \text{ g/L}$ ,  $[\text{PMS}]_0 = 0.2 \text{ mM}$ , initial pH 7.0,  $T = 30^\circ\text{C}$ ).

The photocatalytic capability of TLFO toward ATZ degradation was further investigated by comparing with different photocatalysts in Vis/catalyst/PMS system, including  $\text{Fe}_2\text{O}_3$ ,  $\text{Fe}_3\text{O}_4$ , LFO, h-TiO<sub>2</sub>, solid  $\text{TiO}_2@\text{LFO}$  and TLFO. As shown in Fig. 5b, the h-TiO<sub>2</sub> nanospheres exhibited limited photocatalytic performance, which might be attributed to the limited photocatalytic reactivity of the h-TiO<sub>2</sub> under visible light. Additionally,  $\text{Fe}_2\text{O}_3$ ,  $\text{Fe}_3\text{O}_4$ , and LFO consisting of Fe(II)/Fe(III) redox couple were chosen to investigate their photocatalytic performance, and approximately 7%, 11%, and 24.8% ATZ were degraded after 120 min, respectively. Since the reduction from Fe(II) to Fe(III) is generally considered as the rate-determining step of PMS activation, the inferior circulation ability of Fe(II)/Fe(III) cycle on the surface of the iron oxide had limited their reactivity [45]. Moreover, the photo-generated charge carriers on the oxides were vulnerable to rapid recombination and lead to inferior Fe(II) regeneration during photocatalysis [46]. Thus, it was speculated that inefficient electron transfer of  $\text{Fe}_2\text{O}_3$ ,  $\text{Fe}_3\text{O}_4$ , and LFO played a role in their poor reactivity. Applying a coating of LFO onto the surface of both solid and hollow  $\text{TiO}_2$  yielded a clear improvement in the ATZ degradation. In particular, the hollow-structured TLFO achieved complete ATZ degradation within

90 min with substantially higher degradation rates (Fig. S6). Generally, the hollow structure combined with three-dimensional heterojunction between the LFO shell and hollow  $\text{TiO}_2$  core might synergistically lead to enhanced activity. The underlying mechanism of the photocatalytic degradation process needs further scrutinization.

### 3.3. Effect of parameters

#### 3.3.1. Effect of photocatalyst dosage

As shown in Fig. 7a, various dosages of TLFO ranging from 0.1 g/L to 0.5 g/L were used in the photocatalytic treatment of ATZ to explore the effect of catalyst dosage. When the catalyst dosage increased from 0.1 g/L to 0.4 g/L, the degradation efficiency increased from 51.4% to 100% after 90 min. The highest removal of ATZ was achieved at a dosage of 0.4 g/L due to the abundance of active sites on the surface of the catalyst, enabling sufficiently high amount of reactive species to degrade ATZ. A further increase in the dosage to 0.5 g/L did not result in a remarkably enhanced degradation rate. Moreover, the solution turned opaque due to higher concentrations of TLFO, which might be unfavorable for sufficient light utilization [47]. Therefore, a dosage of

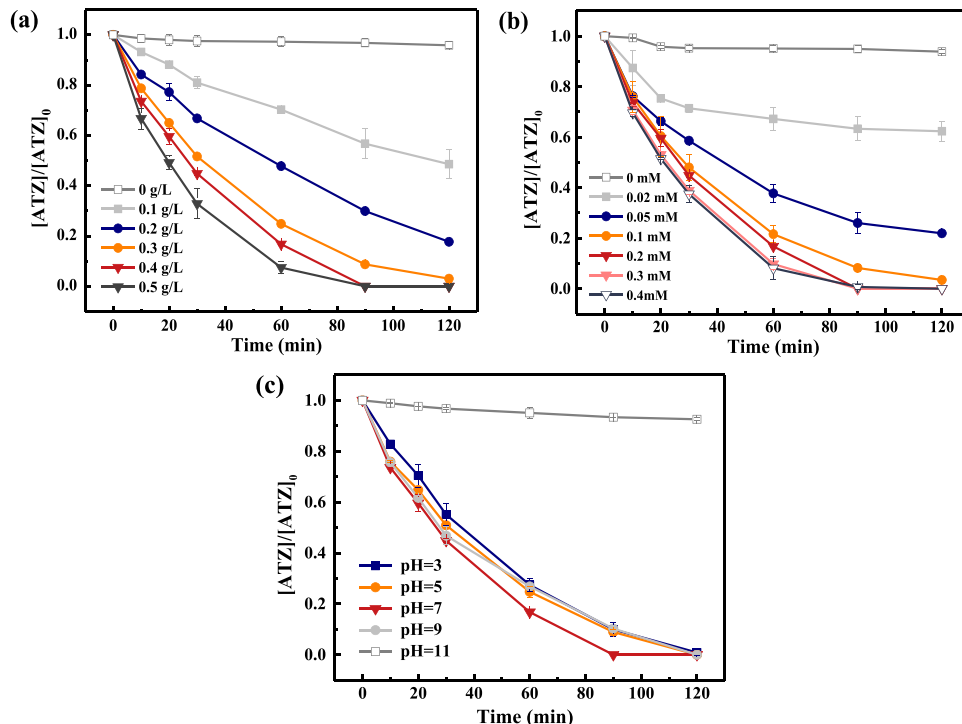


**Fig. 7.** Effects of (a) TLFO photocatalyst dosage, (b) PMS concentration, and (c) initial pH on ATZ photodegradation in Vis/TLFO/PMS system.

0.4 g/L was selected as the optimal photocatalyst concentration.

### 3.3.2. Effect of PMS concentration

According to the U.S environmental protection agency, the maximum permissible level for sulfate in drinking water is 250 mg/L, which corresponds to around 400 mg/L (0.65 mM) of PMS dosage [48]. In this regard, the effect of PMS concentration limited in the range of 0–0.4 mM on ATZ removal was studied. As shown in Fig. 7b, the degradation rate markedly increased from 37.7% to 100% with increasing PMS concentration from 0.02 to 0.2 mM after 120 min. Small concentrations of PMS not only failed to generate sufficient amount of reactive species, but also capture photogenerated electrons for ATZ degradation. With the increase of PMS concentration, a firmer contact was achieved between PMS and TLFO, which favors ROS generation and electron capture process to suppress the recombination of charge carriers. However, no significant improvement in ATZ degradation was observed by further increasing the PMS concentration beyond 0.2 mM. Considering the operating costs and the issue of secondary pollution, a PMS concentration of 0.2 mM was chosen for the subsequent photocatalytic degradation process.

### 3.3.3. Effect of initial pH

As shown in Fig. 7c, pH of the solution is another factor that may affect the PMS activation process and photocatalysis. Complete ATZ degradation was observed at the initial pH values ranging from 3.0 to 9.0 within 120 min pointing to excellent activity for ATZ degradation over a wide pH range in comparison with traditional Fenton reactions that are highly dependent on solution pH [49]. Specifically, the ATZ degradation rate increased with an increase of the initial pH from 3.0 to 7.0, and decreased slightly when the pH changed from 7.0 to 9.0. It was reported that the form of PMS was dependent on the pH of the solution [49]. The  $pK_{a1}$  value of PMS was less than 0, whereas the  $pK_{a2}$  is 9.4. Under acidic and neutral conditions, PMS exists in the main form of  $\text{HSO}_5^-$ , which could be activated to form  $\text{SO}_4^{\bullet-}$  to oxidize ATZ. Furthermore,  $\text{HSO}_5^-$  could react with  $\text{H}_2\text{O}$  or  $\text{OH}^-$  to form  $\bullet\text{OH}$  through Eq. (2) and Eq. (3), which contribute to complete ATZ degradation

within the initial pH range of 3.0–9.0. However, the ATZ degradation was dramatically inhibited at an initial solution pH of 11.0. This is because at high pH of 11, PMS mainly exists as  $\text{SO}_5^{2-}$  that has a limited capability of  $\text{SO}_4^{\bullet-}$  generation. In addition, the photocatalytic reaction could be dramatically impeded due to the scavenging of  $\text{OH}^-$  for photogenerated holes in high pH values [50]. Therefore, the PMS-assisted photodegradation of ATZ was significantly inhibited at extremely high pH of 11.

### 3.3.4. Effect of co-existing ions

Natural water contains various kinds of inorganic anions and natural organic materials (NOM), thus several common anions ( $\text{NO}_3^-$ ,  $\text{Cl}^-$  and  $\text{HCO}_3^-$ ) and humic acid (HA) were chosen to investigate the effect of them on ATZ degradation individually. As shown in Fig. 8, the presence inorganic anions leads to different degrees of inhibition, and the inhibition effect follows the order of  $\text{HCO}_3^- > \text{Cl}^- > \text{NO}_3^-$ . With the increase of  $\text{NO}_3^-$  concentration from 1 to 10 mM, a slight inhibition was observed in the degradation activity. This phenomenon could be explained by the scavenging by  $\text{NO}_3^-$  of ROS generated via Vis/TLFO/PMS system through electron transfer reaction, and the oxidation capacity of the formed nitrate radical ( $\text{NO}_3^{\bullet}$ ), which is relatively weaker (2.3–2.5 V) (Eq. (4) and Eq. (5)) [51]. However, the reaction rates of  $\text{NO}_3^-$  with  $\text{SO}_4^{\bullet-}$  and  $\bullet\text{OH}$  are generally lower than that of ATZ [47].  $\text{Cl}^-$  showed a slight inhibition effect in ATZ degradation in Vis/TLFO/PMS system, which might be ascribed to its competition with ATZ for the generated  $\text{SO}_4^{\bullet-}$  and  $\bullet\text{OH}$ , leading to the formation of  $\text{Cl}^{\bullet}$  (2.03 V) and  $\text{HOCl}^{\bullet-}$  (1.49 V) featuring lower redox potentials [52] (Eqs. (6–8)). Meanwhile,  $\text{Cl}^-$  can act as scavengers of photogenerated holes, which may hinder further generation of  $\bullet\text{OH}$  [53]. It can be observed from Fig. 8c that the presence of  $\text{HCO}_3^-$  exerted an obvious inhibitory effect on the ATZ degradation efficiency in Vis/TLFO/PMS system, which can be ascribed to the radical quenching reactions between  $\text{HCO}_3^-$  and ROS to generate  $\text{HCO}_3^{\bullet-}$  (1.7 V) with less reactivity (Eq. (9) and Eq. (10)). Moreover,  $\text{HCO}_3^-$  could also act as a metal complexing agent to change the surface properties of TLFO, thus inhibiting the redox cycles for ATZ degradation process [54].

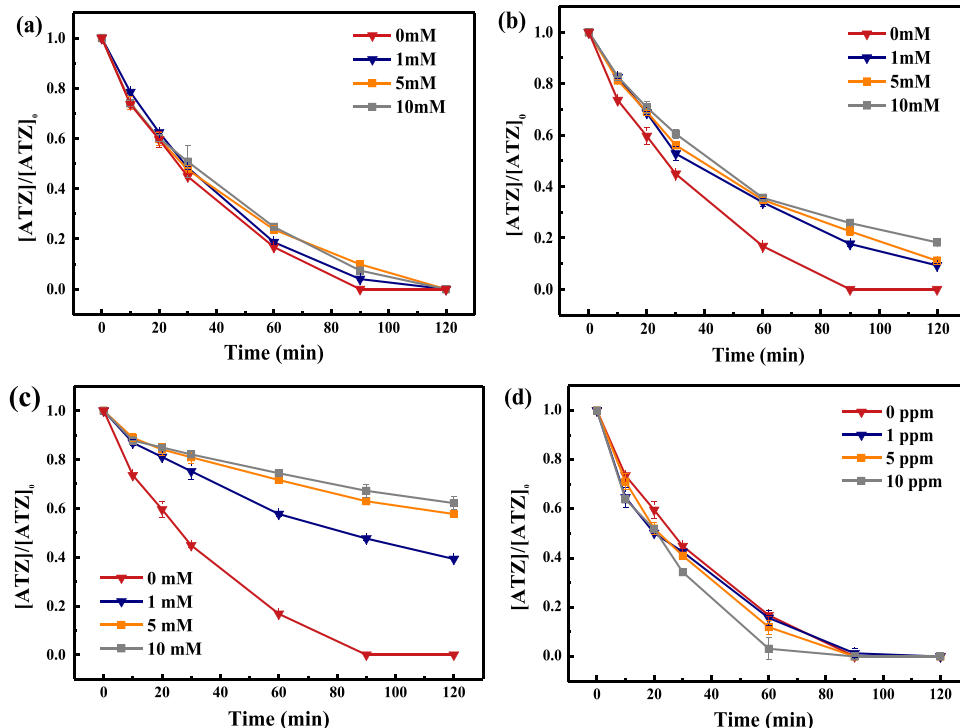
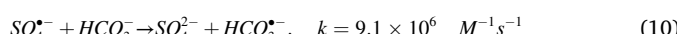
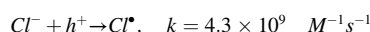
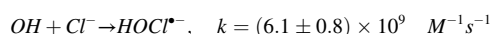
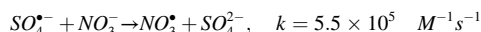
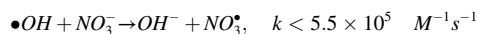
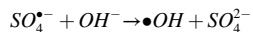


**Fig. 8.** Effects of inorganic anions and organic materials on ATZ photodegradation in Vis/TLFO/PMS system: (a)  $\text{NO}_3^-$ , (b)  $\text{Cl}^-$ , (c)  $\text{HCO}_3^-$ , and (d) humic acid (HA).



HA was chosen as the representative material to investigate the effect of NOM on ATZ removal. According to previous studies,  $SO_4^{\bullet-}$  and  $\bullet OH$  could be scavenged by HA and showed detrimental effect on pollutants degradation [55]. However, it was presented in Fig. 8d that with the HA concentration increasing from 0 to 10 ppm, the ATZ photodegradation rates were promoted to 100% within a treatment duration of 60 min, which could be attributed to the intrinsic photochemical impact of HA under visible light. It was reported that the phenolic groups of HA could act as electron donors and the quinone moieties play the role of electron transferring shuttle between the PMS and HA, thus activating PMS to generate more reactive species [56].

### 3.4. Mechanism

#### 3.4.1. Reactive species and band structure

To explore the photocatalytic mechanism and the major radicals generated in Vis/TLFO/PMS system, several quenching experiments

were conducted using EtOH, TBA, BQ, EDTA-2Na and FFA as ROS scavengers. The impacts of various scavengers on ATZ degradation efficiency were shown in Fig. 9. EtOH is regarded as scavenger for both  $SO_4^{\bullet-}$  and  $\bullet OH$  ( $k_1(SO_4^{\bullet-}, \text{EtOH}) = 1.6-7.7 \times 10^7 \text{ M}^{-1}\text{s}^{-1}$  and  $k_1(\bullet OH, \text{EtOH}) = 1.2-2.8 \times 10^9 \text{ M}^{-1}\text{s}^{-1}$ ) with  $\alpha$ -hydrogen, while TBA was selected to scavenge  $\bullet OH$  only ( $k_1(SO_4^{\bullet-}, \text{TBA}) = 4 \times 10^5 \text{ M}^{-1}\text{s}^{-1}$  and  $k_1(\bullet OH, \text{TBA}) = 3.8-7.6 \times 10^8 \text{ M}^{-1}\text{s}^{-1}$ ) [57]. When 200 mM EtOH and TBA were introduced into the solution, the ATZ removal efficiency was reduced from 100% to 8% and 29%, respectively, demonstrating that both  $\bullet OH$  and  $SO_4^{\bullet-}$  were involved in the Vis/TLFO/PMS system, and  $\bullet OH$  played a more dominant role as compared with  $SO_4^{\bullet-}$  in ATZ photodegradation process. In addition to the contribution of  $SO_4^{\bullet-}$  and  $\bullet OH$ , the role of other active species including  $O_2^{\bullet-}$ ,  $^1O_2$  and photo-generated holes were also evaluated. A decline to 57% ATZ removal rate was witnessed after the addition of 5 mM BQ, which might be attributed to the presence of  $O_2^{\bullet-}$  ( $k_1(O_2^{\bullet-}, \text{BQ}) = 1.0 \times 10^9 \text{ M}^{-1}\text{s}^{-1}$ ) that contributed to ATZ degradation. However, BQ can also react with other reactive species and the existence of  $O_2^{\bullet-}$  should be further confirmed by in-situ EPR analysis. The contribution of photogenerated  $h^+$  was evaluated using 5 mM EDTA-2Na as tapping agent, and the most significant suppression, yielding approximately 93.4% declined in ATZ removal was observed, indicating the crucial role of  $h^+$  in PMS-assisted photodegradation of ATZ. On account of the strong oxidizing ability of  $h^+$  that  $h^+$  could both directly oxidize ATZ and react with  $H_2O$  to produce more  $\bullet OH$  [58]. Further, the contribution of singlet oxygen ( $^1O_2$ ) was evaluated by introducing 5 mM FFA into the Vis/TLFO/PMS system. The results showed the ATZ removal efficiency was significantly reduced to 3% with addition of FFA. It is worth noting that FFA could react rapidly with both  $^1O_2$  and  $\bullet OH$  ( $k_1(\bullet OH, \text{FFA}) = 1.5 \times 10^{10} \text{ M}^{-1}\text{s}^{-1}$  and  $k_1(^1O_2, \text{FFA}) = 1.2 \times 10^8 \text{ M}^{-1}\text{s}^{-1}$ ) [59]. To verify the involvement of generated  $^1O_2$  on ATZ degradation, experiments were conducted in  $^1O_2$ -photogenerated visible light/rose Bengal system (Fig. S7), which showed ATZ could be partially oxidized by  $^1O_2$  despite its high selectivity towards organic compound and relatively low

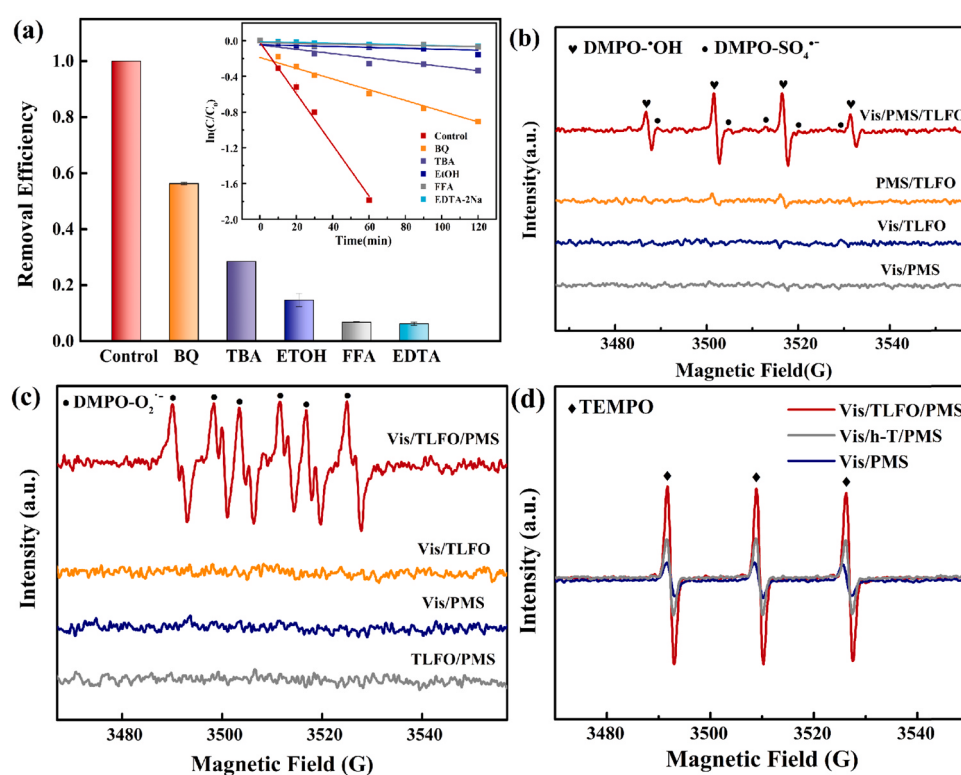


**Fig. 9.** (a) Effects of different ROS scavengers for ATZ photodegradation in the Vis/TLFO/PMS system, and (b–d) EPR spectra of different systems with DMPO or TEMP as the trapping agents.

redox potential (0.81 V) [60,61]. This result was in line with the previous reported work that proved the electron-rich group in ATZ could be oxidized by  $^1\text{O}_2$  [62]. Therefore, it was speculated that both  $\cdot\text{OH}$  and  $^1\text{O}_2$  contributed to ATZ removal in the PMS-assisted TLFO photolysis process, which requires further verifying by EPR spectroscopy.

To confirm the existence of these ROS, EPR spectroscopy was conducted with DMPO and TEMP as the spin-trapping reagent. As shown in Fig. 9b, the signal of DMPO- $\cdot\text{OH}$  and DMPO- $\text{SO}_4^{2-}$  adducts can be observed in Vis/TLFO/PMS system. The results provided direct evidence to the existence and contribution of  $\cdot\text{OH}$  and  $\text{SO}_4^{2-}$  in the Vis/TLFO/PMS system. By contrast, weak DMPO- $\cdot\text{OH}$  signal was observed in the TLFO/PMS and Vis/TLFO systems, indicating the superior synergistic effect of PMS and TLFO under visible light illumination in the Vis/TLFO/PMS system, which was in accordance with previous ATZ degradation rates. Since visible light was unable to initiate the direct homolysis of PMS, no distinct signals were observed in Vis/PMS system [63]. In addition, the presence of  $\text{O}_2^{2-}$  was confirmed according to the characteristic peak of DMPO- $\text{O}_2^{2-}$  obtained distinctly in the Vis/TLFO/PMS system, implying  $\text{O}_2^{2-}$  was produced and contributed to the ATZ destruction. However, there was no DMPO- $\text{O}_2^{2-}$  signal obtained in other systems, suggesting the generation of  $\text{O}_2^{2-}$  was induced by the electrons excited on the VB of TLFO under visible light irradiation (Fig. 9c). Besides, EPR results in Fig. 9d showed typical characteristic triple peaks of  $^1\text{O}_2$  in the Vis/TLFO/PMS system. For comparison, barely illuminating PMS solution under visible light also led to the weak TEMPO peaks, which was ascribed to  $^1\text{O}_2$  generation via PMS self-decomposition [64]. Additionally, the intensity of TEMPO in the Vis/TLFO/PMS system was much higher than that of Vis/h-TiO<sub>2</sub>/PMS, indicating that the LFO shell on the surface of TLFO might facilitate the PMS self-decomposition and lead to  $^1\text{O}_2$  generation (Eq. (11)) [65]. Meanwhile,  $\text{O}_2^{2-}$  produced in the Vis/TLFO/PMS system could also lead to  $^1\text{O}_2$  generation (Eq. (12)) [66]. Therefore, it can be concluded that ATZ photodegradation was governed by both radical and non-radical species according to results of the quenching experiments and EPR analysis, including  $\cdot\text{OH}$ ,  $\text{h}^+$ ,  $\text{SO}_4^{2-}$ ,  $\text{O}_2^{2-}$ , and  $^1\text{O}_2$  in the PMS-assisted photocatalysis process.



To further understand the charge transfer mechanism across the heterojunctions for reactive species generation, the band structure of LFO and h-TiO<sub>2</sub> was calculated by Mott-Schottky measurement (Eq. (13)), where the  $N_d$  denotes the carrier density,  $C$ ,  $E$ , and  $E_{FB}$  denote the space charge capacitance, applied potential, and the flat band potential, respectively.  $T$  denotes the temperature,  $K_b$  denotes the Boltzmann constant,  $e$  denotes the elemental charge, and  $\epsilon_0$  denotes the vacuum permittivity [21].

As presented in Fig. 10, the slope in the linear region of the plot is positive for h-TiO<sub>2</sub>, indicating that it belongs to n-type semiconductor,

while the slope for LFO is negative, indicating that the synthesized LFO is a p-type semiconductor [67]. In addition, the flat band potential is calculated by the x-axis intercept of MS plots, which is  $-0.58$  eV for h-TiO<sub>2</sub> and  $2.10$  eV for LFO (vs. SCE). According to Eqs. (14–16), it can be deduced that the VB of LFO and CB of h-TiO<sub>2</sub> locate at about  $2.44$  eV and  $-0.34$  eV (vs. NHE), respectively [68]. Combined with above analysis, the band structure of TLFO consisting of the two semiconductors and the ROS generation process in Vis/TLFO/PMS are illustrated in Fig. 11.

$$\frac{1}{C^2} = \pm \frac{2}{e\epsilon\epsilon_0 N_d} (E - E_{FB} - \frac{K_b T}{e}) \quad (13)$$

$$E(\text{vs. NHE}) = E(\text{vs. NHE}) + 0.244 \text{ eV} \quad (14)$$

$$VB_{LFO} = E_{FB} + 0.1 \text{ eV} \quad (15)$$

$$CB_{h-\text{TiO}_2} = E_{FB} \quad (16)$$

When h-TiO<sub>2</sub> and LFO were in direct contact within TLFO photocatalyst, electrons spontaneously immigrated from h-TiO<sub>2</sub> to LFO owing to the nonequilibrium between the fermi level of the two semiconductors, and induced an accumulation of positive charge and negative charge accumulation at the interface of h-TiO<sub>2</sub> and LFO, respectively. Thus, an internal electric field at the core-shell interface would be constructed [69–71]. Consequently, the photogenerated electrons of LFO within TLFO would transfer to the CB of h-TiO<sub>2</sub> with driving force of the built-in electric field, concurrently leaving the photogenerated holes at VB of LFO. The visible-light excited electrons to TiO<sub>2</sub> with more negative CB value were expected to possess more energy to induce reduction reactions of O<sub>2</sub>. Thus, the recombination of charge carriers was restrained and more electrons and holes were available for photodegradation due to the formed p-n heterojunction.

### 3.4.2. Possible photocatalytic mechanism in Vis/TLFO/PMS system

When TLFO was under visible light irradiation, the photosensitive LFO shell could harvest photons possessing energies of more than  $2.56$  eV and induce electron excitation to CB. These electrons would transfer to h-TiO<sub>2</sub> under internal electric field and accumulate on the CB, realizing the light utilization extended to visible region (Eq. (17)). Combined with the previous bandgap calculation, the electron-rich CB of TiO<sub>2</sub> with a high enough position ( $-0.34$  eV vs. NHE) would induce reduction of O<sub>2</sub> and O<sub>2</sub><sup>2-</sup> generation over TLFO (Eq. (18)). Simultaneously, photogenerated holes leaving VB of LFO ( $2.44$  eV vs. NHE) would further allow the oxidation reaction of H<sub>2</sub>O ( $2.27$  eV vs. NHE) with the generation of  $\cdot\text{OH}$  to participate in ATZ removal, as well as directly lead to ATZ degradation via oxidizing  $\text{h}^+$  (Eq. (19) and Eq. (20)).

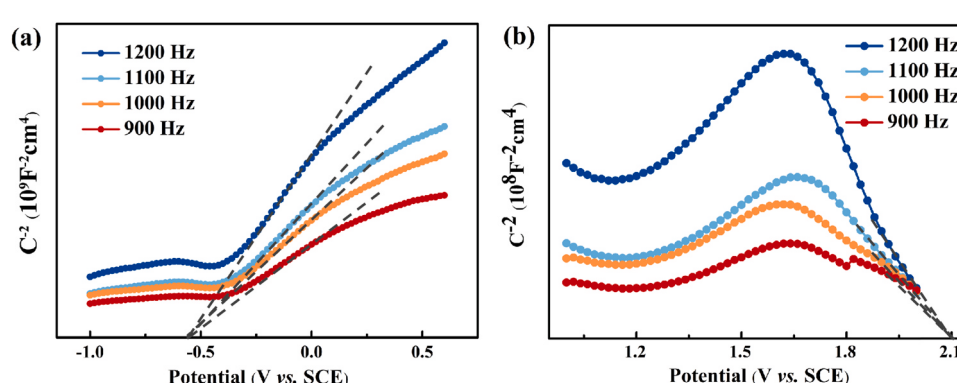


Fig. 10. Mott-Schottky measurement of the photocatalysts: (a) h-TiO<sub>2</sub>, and (b) LFO.

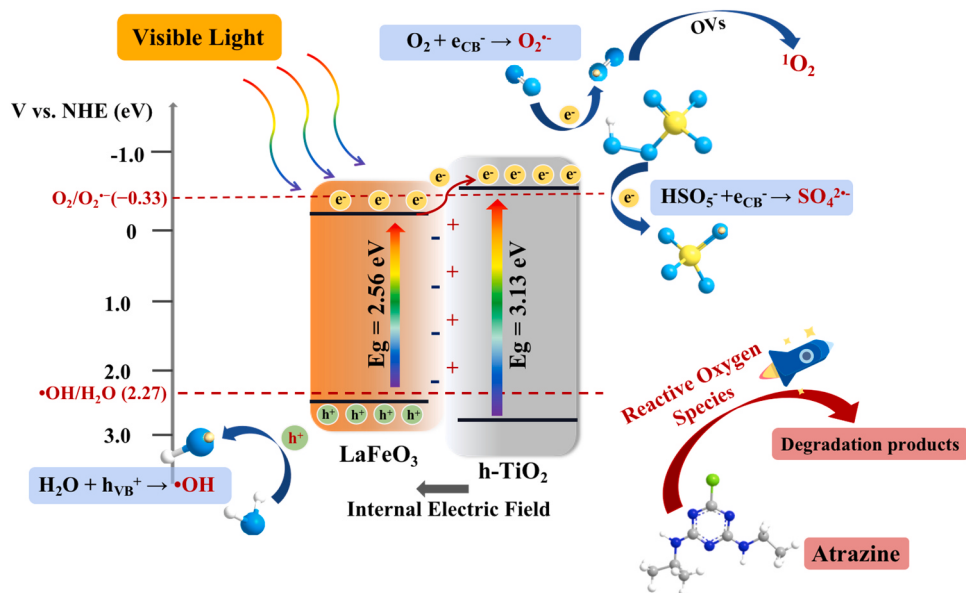


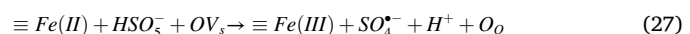
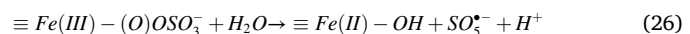
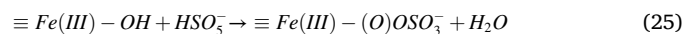
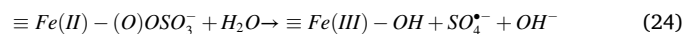
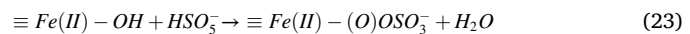
Fig. 11. Schematic illustration of the band structure of TLFO and ROS generation process in Vis/TLFO/PMS system.



In addition, PMS promoted ATZ degradation in the Vis/TLFO/PMS system for it served dually as electron trapper and radical precursor, allowing for the photogenerated charge to be efficiently captured by PMS to initiate ROS production. On the other hand, photogenerated electrons over TLFO photocatalyst could combine with PMS and break the peroxide bond to form SO<sub>4</sub><sup>•-</sup> (Eq. (21)). However, SO<sub>4</sub><sup>•-</sup> was not the dominant oxidant in the Vis/TLFO/PMS system. Consequently, it was concluded that the presence of PMS mainly induced continuous extraction of photogenerated electrons through three-dimensional channels, which inhibited the electron-hole recombination and energy loss during photocatalysis. Thus, the lifetime of photogenerated charge carriers can be prolonged, and more holes are available for OH<sup>•</sup> generation and pollutants removal. The PMS utilization in different processes during treatment was evaluated to prove the efficient activation of PMS in the Vis/TLFO/PMS system as compared to the Vis/PMS and TLFO/PMS systems. The residual PMS concentration in solution was determined by an ABTS colorimetric method as depicted in Test S5 [72]. According to Fig. S8, the PMS consumption was positively related to the reaction time in the Vis/TLFO/PMS system, and the residual concentration declined to 0.11 mM after 120 min treatment. In comparison, Vis/PMS and TLFO/PMS system showed similar trend in PMS decomposition, resulting in 13.6% and 17.8% PMS consumption, respectively. The results demonstrated that PMS could capture photogenerated electrons from TLFO that were driven from the internal electric field across the heterojunction under visible light to inhibit charge carriers' recombination. However, the active sites for useful PMS utilization and ROS generation in Vis/PMS and TLFO/PMS system were limited, which resulted in ineffective PMS utilization and ATZ decontamination [73, 74].

Fe(II) on the surface of TLFO was also capable of initiating PMS to form SO<sub>4</sub><sup>•-</sup> and OH<sup>•</sup>, and it would firstly form bonds with water molecules and then react with PMS to form Fe(II)-(O)OSO<sub>3</sub><sup>-</sup> compound (Eq. (22) and Eq. (23)) [75]. Since the standard reduction potential of Fe(III)/Fe(II) (+0.77 V) is more negative than HSO<sub>5</sub><sup>-</sup>/SO<sub>4</sub><sup>•-</sup> (+2.6–3.1 V),

activation of PMS by Fe(II) to produce SO<sub>4</sub><sup>•-</sup> via reduction was thermodynamically favored (Eqs. (24–26)) [76]. In addition, surface oxygen vacancies within LFO according to XPS analysis, as Lewis acid sites for accepting electrons, could promote the connection between photocatalyst and PMS, providing channels for electron transfer from Fe(II) to activate PMS and form normal oxygen ion (O<sub>2</sub>) [77–79]. In this way, PMS self-decomposition was promoted by oxygen vacancies within TLFO via lowering the reaction barrier and contributed to abundant O<sub>2</sub><sup>•</sup> generation as well as the non-radical degradation pathway of ATZ (Eqs. (27–28)), which was quantitatively demonstrated with EPR analysis of O<sub>2</sub><sup>•</sup> generation comparing Vis/TLFO/PMS system with hollow TiO<sub>2</sub> and non-photocatalyst systems that exhibited lower degradation efficiency. Moreover, the formation of O<sub>2</sub><sup>•</sup> in Vis/TLFO/PMS system might also arise from excessive O<sub>2</sub><sup>•-</sup> and responsible for ATZ degradation (Eq. (29)) [80].



Structurally, the hollow interior space and core-shell morphology of TLFO provided larger surface area and channels compared with solid spheres, which shortened the diffusion paths for the reactants and endowed accelerated ROS generation for enhanced ATZ removal rate on the active sites. Additionally, growing LFO shell on the surface of hollow TiO<sub>2</sub> enabled a close contact at the intermediate layer and facilitated the transfer of photogenerated electrons through the three-dimensional heterojunction, which leads to efficient charge separation to directly activate PMS without compromising active species on TLFO.

### 3.4.3. ATZ degradation pathway

ATZ degradation in the Vis/TLFO/PMS system was studied using LC/MS. Multiple degradation intermediates were observed (Table S1), and the possible degradation pathways were proposed accordingly. As revealed in Fig. 12, ATZ underwent degradation pathways including (i) de-alkylation; (ii) alkyllic-hydroxylation and (iii) dechlorination-hydroxylation [81].

ATZ could be degraded directly through de-alkylation reaction in the presence of photogenerated ROS, and generated dealkylated ATZ derivatives including 2-chloro-4-amino-6-isopropylamino-1,3,5-triazine (CAIT  $m/z$  188), 2-chloro-4-ethylamino-6-amino-s-triazine (CEAT  $m/z$  174), and 2-chloro-4,6-diamino-1,3,5-triazine (CAAT  $m/z$  146) via deethylation and deisopropylation. This was in accordance with previous studies which have proved that C-N bond in the lateral chains could be easily cleaved with relatively low bond energy, resulting in the yield of dealkylation products [82]. As for alkyllic-hydroxylation process, ROS would attack the carbon atoms and induce hydrogen atom abstraction on the ethylamino or iso-propylamino chains next to a nitrogen atom of ATZ. Especially, H-abstraction induced by  $\bullet$ OH could easily overcome small energy barriers with only 2.02 kcal/mol and 1.72 kcal/mol for ethyl group and isopropyl group, respectively. The formed carbon-centered radicals could further combine with  $\bullet$ OH and lead to hydroxylated intermediates 1-((4-chloro-6-(isopropylamino)-1,3,5-triazin-2-yl)amino) ethan-1-ol (CNIT  $m/z$  232) and 2-((4-chloro-6-(ethylamino)-1,3,5-triazin-2-yl)amino) propan-2-ol (CNET  $m/z$  232). These products would further undergo decomposition process including dealkylation through cleavage of C-N bonds, leading to the generation of CAIT and CEAT, respectively. During this degradation process, water molecules would act as a catalyst to shuttle H atoms from -OH groups to N atoms so as to reduce the reaction barrier dramatically to realize the reaction pathway [83]. Simultaneously, photogenerated ROS further attacked alkyllic-hydroxylation product CNIT accompanied by the H-abstraction reaction and produced aldehyde intermediate N-(4-chloro-6-(isopropylamino)-1,3,5-triazin-2-yl)acetamide (CDIT  $m/z$  230).

Additionally, photogenerated  $\bullet$ OH was expected to attack the C atom attached to chlorine in the aromatic ring and induce a nucleophilic substitution, thus leading to the dechlorination-hydroxylation reactions. Thus, degradation intermediates such as N-(4-(ethylamino)-6-hydroxy-1,3,5-triazin-2-yl)acetamide (ODIT  $m/z$  212) and 4,6-diamino-1,3,5-triazin-2-ol (OAAT  $m/z$  128) without Cl atom were formed via the cleavage

of C-Cl bond and  $\bullet$ OH adduct. Moreover, the cleavage of C-N in ethylamino of ODIT could be easily initiated due to its low bond energy to produce 4-amino-6-(isopropylamino)-1,3,5-triazin-2-ol (OAAT  $m/z$  170), and finally transformed to OAAT via iso-propylamino deprivation, which could be further mineralized to smaller compounds such as  $\text{CO}_2$  and  $\text{H}_2\text{O}$ . Consequently, the oxidative degradation based on photo-generated ROS in Vis/TLFO/PMS system can greatly reduce the toxicity of ATZ or even convert it to some nontoxic products, confirming TLFO as a potential photocatalyst for promoting ATZ degradation to less harmful species, which could possibly be applicable to other toxic organic herbicides.

### 3.5. Reusability and stability

For the practical applications of a heterogeneous photocatalyst, the durability and stability are critical factors. Therefore, the cycle experiment for ATZ photodegradation was carried out to investigate the reusability of the TLFO. After each run, the used photocatalyst was recovered via filtration and distilled water washing, whose performance was depicted in Fig. 13. It was found that complete ATZ oxidation could be achieved within 120 min for the seven subsequent cycles, revealing no sign of deactivation. The superior reusability of TLFO demonstrating the contribution of the stable TLFO heterojunction and built-in electric field as charge transfer driving force to enhance photoreactivity for ATZ removal in the Vis/TLFO/PMS system. Interestingly, the removal rate of ATZ in the Vis/TLFO/PMS system showed a slight increase compared to the fresh TLFO from the fourth cycle onwards. According to the TEM image of the TLFO after six cycles (Fig. 3e), the used TLFO nanospheres appeared to be partially broken, and a tiny aperture was created presenting a bowl-like hollow structure. This unique broken 3D spherical core-shell structure favored the light reflection and scattering in the interiors of TLFO [84]. Furthermore, better permeability of the broken structure was also beneficial for the transport of pollutants and reactants from the inner and outer exposed surfaces with active sites, further contributing to the enhanced ATZ removal rates [85]. Moreover, Fe and La leaching of TLFO were detected to be below 0.01 mg/L during the photodegradation process, suggesting excellent stability and durability of TLFO. In general, the advanced photocatalytic activity of TLFO was attributed to the hierarchical core-shell heterojunction and enhanced electron transfer and utilization, allowing for excellent structural stability and durable photoactivity in ATZ photodegradation.

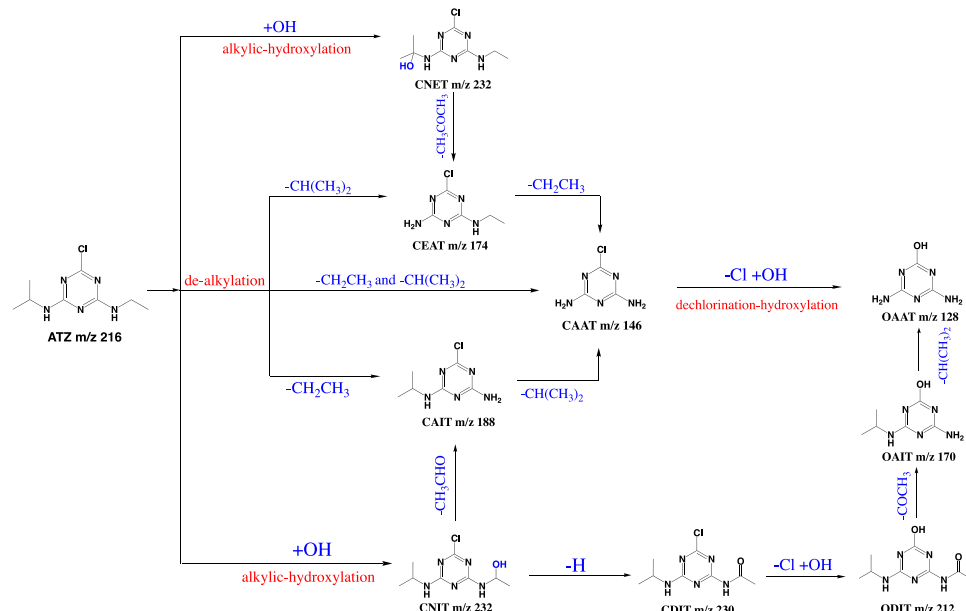
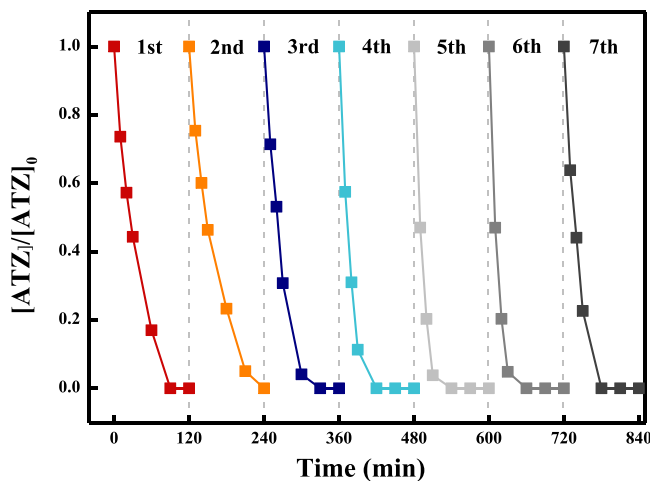


Fig. 12. Possible pathways of ATZ photodegradation in the Vis/TLFO/PMS system.



**Fig. 13.** Reusability of TLFO in the Vis/TLFO/PMS system for ATZ photo-degradation process.

#### 4. Conclusion

In summary, a novel heterojunction with three-dimensional hollow core-shell structure (TLFO) was developed via a facile method, and the as-prepared heterojunction was found to be highly effective for ATZ photodegradation within 90 min with the assistance of PMS. The experimental results and characterization analysis both demonstrated the contribution of  $\cdot\text{OH}$ ,  $\text{h}^+$ ,  $\text{SO}_4^{2-}$ , and  $\text{O}_2^{2-}$  and  ${}^1\text{O}_2$  in ATZ removal. This novel hollow core-shell heterojunction exhibited efficient visible light utilization, and the built-in electric field originated from the two semiconductors acted as the charge transfer driving force to maximum electron transfer and ROS generation, which contributed to efficient ATZ removal. Besides, PMS served dually as reactive species precursor and electron acceptor, to capture photogenerated  $\text{e}^-$  to initiate  $\text{SO}_4^{2-}$  generation and leave  $\text{h}^+$  to be available for  $\cdot\text{OH}$  generation during photocatalysis. Furthermore, TLFO showed environmentally friendly advantages such as long-term stability and resistance to metal leaching throughout reused process. In general, this study provides a promising strategy to fabricate novel durable heterojunction photocatalyst with enhanced charge separation efficiency in PMS-assisted photodegradation for the highly effective removal of pollutants from wastewater.

#### CRediT authorship contribution statement

**Kexin Wei:** Data curation, Formal analysis, Writing – original draft, Visualization. **Andac Armutlulu:** Conceptualization, Writing – review & editing. **Yinxu Wang:** Data curation, Validation. **Gang Yao:** Supervision. **Ruzhen Xie:** Conceptualization, Methodology, Validation, Project administration, Funding acquisition. **Bo Lai:** Validation, Conceptualization, Funding acquisition.

#### Acknowledgments

The authors acknowledge the funding support from the National Natural Science Foundation of China (No. 52170089, No. 51808360), and Chengdu Science and Technology Department (2019-GH02-00053-HZ). We would also like to thank Hanjiao Chen (EPR), Bo Gao (LC-MS), and Hui Wang (SEM) from Analytical & Testing center of Sichuan University for their support.

#### Declaration of Competing Interest

The authors declare that they have no known competing financial interests or personal relationships that could have appeared to influence

the work reported in this paper.

#### Appendix A. Supporting information

Supplementary data associated with this article can be found in the online version at doi:10.1016/j.apcatb.2021.120889.

#### References

- [1] R. Zhang, J. Du, X. Dong, Y. Huang, H. Xie, J. Chen, X. Li, K. Kadokami, Occurrence and ecological risks of 156 pharmaceuticals and 296 pesticides in seawater from marine areas of Northeast China, *Sci. Total Environ.* 792 (2021), 148375.
- [2] N. Rousis, E. Gracia-Lor, H. Félix, F. Poretti, S. Castiglioni, Wastewater-based epidemiology as a novel tool to evaluate human exposure to pesticides: triazines and organophosphates as case studies, *Sci. Total Environ.* 793 (2021), 148618.
- [3] B. Wu, W.A. Arnold, L. Ma, Photolysis of atrazine: role of triplet dissolved organic matter and limitations of sensitizers and quenchers, *Water Res.* 190 (2021), 116659.
- [4] R. Supe, W. Ouyang, X. Gu, C. Lin, M. Tysklind, B. Wang, Typical herbicide residues, trophic transfer, bioconcentration, and health risk of marine organisms, *Environ. Int.* 152 (2021), 106500.
- [5] J. Li, Y.J. Li, Z.K. Xiong, G. Yao, B. Lai, The electrochemical advanced oxidation processes coupling of oxidants for organic pollutants degradation: a mini-review, *Chin. Chem. Lett.* 30 (2019) 2139–2146.
- [6] Z. Feng, Q. Tian, Q. Yang, Y. Zhou, H. Zhao, G. Zhao, Selectively photoelectrocatalytic reduction of oxygen to hydroxyl radical and singlet oxygen: mechanism and validation in coal wastewater, *Appl. Catal. B Environ.* 286 (2021), 119908.
- [7] K. Pan, C. Yang, J. Hu, W. Yang, B. Liu, J. Yang, S. Liang, K. Xiao, H. Hou, Oxygen vacancy mediated surface charge redistribution of Cu-substituted LaFeO<sub>3</sub> for degradation of bisphenol A by efficient decomposition of H<sub>2</sub>O<sub>2</sub>, *J. Hazard. Mater.* 389 (2020), 122072.
- [8] H. Lutze, S. Bircher, I. Rapp, N. Kerlin, R. Bakkour, M. Geisler, C. von Sonntag, T. Schmidt, Degradation of chlorotriazine pesticides by sulfate radicals and the influence of organic matter, *Environ. Sci. Technol.* 49 (2015) 1673–1680.
- [9] J. Li, J.F. Yan, G. Yao, Y.H. Zhang, X. Li, B. Lai, Improving the degradation of atrazine in the three-dimensional (3D) electrochemical process using CuFe2O4 as both particle electrode and catalyst for persulfate activation, *Chem. Eng. J.* 361 (2019) 1317–1332.
- [10] D. Tian, H. Zhou, H. Zhang, P. Zhou, B. Lai, Heterogeneous photocatalyst-driven persulfate activation process under visible light irradiation: from basic catalyst design principles to novel enhancement strategies, *Chem. Eng. J.* 428 (2021), 131166.
- [11] L. Yang, X. Bai, J. Shi, X. Du, L. Xu, P. Jin, Quasi-full-visible-light absorption by D35-TiO<sub>2</sub>/g-C3N4 for synergistic persulfate activation towards efficient photodegradation of micropollutants, *Appl. Catal. B Environ.* 256 (2019), 117759.
- [12] L. Achola, A. Ghebrehiwet, J. Macharia, P. Kerns, J. He, J. Fee, C. Tinson, J. Shi, S. March, M. Jain, S. Suib, Enhanced visible-light-assisted peroxymonosulfate activation on cobalt-doped mesoporous iron oxide for orange II degradation, *Appl. Catal. B Environ.* 263 (2020), 118332.
- [13] J. Lim, Y. Yang, M. Hoffmann, Activation of peroxymonosulfate by oxygen vacancies-enriched cobalt-doped black TiO<sub>2</sub> nanotubes for the removal of organic pollutants, *Environ. Sci. Technol.* 53 (2019) 6972–6980.
- [14] H. Qiu, P. Guo, L. Yuan, G. Sheng, Different non-radical oxidation processes of persulfate and peroxymonosulfate activation by nitrogen-doped mesoporous carbon, *Chin. Chem. Lett.* 31 (2020) 2614–2618.
- [15] Y. Jiang, Z. Xiong, J. Huang, F. Yan, B. Lai, Effective E. coli inactivation of core-shell ZnO@ZIF-8 photocatalysis under visible light synergize with peroxymonosulfate: efficiency and mechanism, *Chin. Chem. Lett.*, 2021.
- [16] X. Jiang, Y. Guo, L. Zhang, W. Jiang, R. Xie, Catalytic degradation of tetracycline hydrochloride by persulfate activated with nano Fe-0 immobilized mesoporous carbon, *Chem. Eng. J.* 341 (2018) 392–401.
- [17] P. Guo, H. Qiu, C. Yang, G. Sheng, Highly efficient removal and detoxification of phenolic compounds using persulfate activated by MnO<sub>x</sub>@OMC: synergistic mechanism and kinetic analysis, *J. Hazard. Mater.* 402 (2020), 123846.
- [18] H. Zhang, Q.Q. Ji, L.D. Lai, G. Yao, B. Lai, Degradation of p-nitrophenol (PNP) in aqueous solution by mFe/Cu-air-PS system, *Chin. Chem. Lett.* 30 (2019) 1129–1132.
- [19] K. Wei, Y. Faraj, G. Yao, R. Xie, B. Lai, Strategies for improving perovskite photocatalysts reactivity for organic pollutants degradation: a review on recent progress, *Chem. Eng. J.* 414 (2021), 128783.
- [20] H. Hu, Y. Lin, Y. Hu, Synthesis, structures and applications of single component core-shell structured TiO<sub>2</sub>: a review, *Chem. Eng. J.* 375 (2019), 122029.
- [21] M. Ismael, M. Wark, Perovskite-type LaFeO<sub>3</sub>: photoelectrochemical properties and photocatalytic degradation of organic pollutants under visible light irradiation, *Catalysts* 9 (2019) 342.
- [22] W. Meng, Y. Wang, Y. Zhang, C. Liu, Z. Wang, Z. Song, B. Xu, F. Qi, A. Ikhlaq, Degradation Rhodamine B dye wastewater by sulfate radical-based visible light-fenton mediated by LaFeO<sub>3</sub>: reaction mechanism and empirical modeling, *J. Taiwan Inst. Chem. Eng.* 111 (2020) 162–169.
- [23] M. Ismael, Y. Wu, A facile synthesis method for fabrication of LaFeO<sub>3</sub>/g-C3N4 nanocomposite as efficient visible-light-driven photocatalyst for photodegradation of RhB and 4-CP, *New J. Chem.* 43 (2019) 13783–13793.

- [24] K. Peng, L. Fu, H. Yang, J. Ouyang, Perovskite LaFeO<sub>3</sub>/montmorillonite nanocomposites: synthesis, interface characteristics and enhanced photocatalytic activity, *Sci. Rep.* 6 (2016) 19723.
- [25] G. Fan, Z. Chen, Z. Yan, B. Du, H. Pang, D. Tang, J. Luo, J. Lin, Efficient integration of plasmonic Ag/AgCl with perovskite-type LaFeO<sub>3</sub>: enhanced visible-light photocatalytic activity for removal of harmful algae, *J. Hazard. Mater.* 409 (2021), 125018.
- [26] S. Nandi, W. Jiang, P. Simon, N. Nuns, E. Berrier, Mn- or Cu- substituted LaFeO<sub>3</sub>-based three-way catalysts: highlighting different catalytically operating modes of La<sub>0.67</sub>Fe<sub>0.8</sub>Mn<sub>0.2</sub>O<sub>3</sub> (M=Cu, Mn), *Appl. Catal. B Environ.* 296 (2021), 120330.
- [27] Y. Wu, H. Wang, W. Tu, Y. Liu, Y.Z. Tan, X.Z. Yuan, J.W. Chew, Quasi-polymeric construction of stable perovskite-type LaFeO<sub>3</sub>/g-C<sub>3</sub>N<sub>4</sub> heterostructured photocatalyst for improved Z-scheme photocatalytic activity via solid p-n heterojunction interfacial effect, *J. Hazard. Mater.* 347 (2018) 412–422.
- [28] P. Garcia-Munoz, F. Fresno, J. Ivaniez, D. Robert, N. Keller, Activity enhancement pathways in LaFeO<sub>3</sub>@TiO<sub>2</sub> heterojunction photocatalysts for visible and solar light driven degradation of myclobutanil pesticide in water, *J. Hazard. Mater.* 400 (2020), 123099.
- [29] K. Saravananumar, M. Chang, Rational design of a novel LaFeO<sub>3</sub>/g-C<sub>3</sub>N<sub>4</sub>/BiFeO<sub>3</sub> double Z-scheme structure: photocatalytic performance for antibiotic degradation and mechanistic insight, *Chem. Eng. J.* 423 (2021), 130076.
- [30] G. Prieto, H. Tuysuz, N. Duyckaerts, J. Knossalla, G. Wang, F. Schuth, Hollow nano- and microstructures as catalysts, *Chem. Rev.* 116 (2016) 14056–14119.
- [31] K. Wang, Z. Xing, D. Meng, S. Zhang, W. Zhou, Hollow MoSe<sub>2</sub>@Bi<sub>2</sub>S<sub>3</sub>/CdS core-shell nanostructure as dual Z-scheme heterojunctions with enhanced full spectrum photocatalytic-photothermal performance, *Appl. Catal. B Environ.* 563 (2020) 119482.
- [32] J. Wang, C. Xue, W. Yao, J. Liu, X. Gao, R. Zong, Z. Yang, W. Jin, D. Tao, MOF-derived hollow TiO<sub>2</sub>@C/FeTiO<sub>3</sub> nanoparticles as photoanodes with enhanced full spectrum light PEC activities, *Appl. Catal. B Environ.* 250 (2019) 369–381.
- [33] Q. Tang, X. An, H. Lan, H. Liu, J. Qu, Polyoxometalates/TiO<sub>2</sub> photocatalysts with engineered facets for enhanced degradation of bisphenol A through persulfate activation, *Appl. Catal. B Environ.* 268 (2019), 118394.
- [34] Z. Pap, V. Danciu, Z. Cegled, A. Kukovecz, A. Oszko, A. Domki, K. Mogyorosi, The influence of rapid heat treatment in still air on the photocatalytic activity of titania photocatalysts for phenol and monuron degradation, *Appl. Catal. B Environ.* 101 (2011) 461–470.
- [35] S. Khanchandani, S. Kumar, A.K. Ganguli, Comparative study of TiO<sub>2</sub>/CuS core-shell and composite nanostructures for efficient visible light photocatalysis, *ACS Sustain. Chem. Eng.* 4 (2016) 1487–1499.
- [36] S. Hammouda, F. Zhao, Z. Safaei, V. Srivastava, D. Ramasamy, S. Iftekhar, S. Kalliola, M. Sillanpaa, Degradation and mineralization of phenol in aqueous medium by heterogeneous monopersulfate activation on nanostructured cobalt based-perovskite catalysts ACoO(3) (A = La, Ba, Sr and Ce): characterization, kinetics and mechanism study, *Appl. Catal. B Environ.* 215 (2017) 60–73.
- [37] X. Wang, X. Pu, Y. Yuan, Y. Xiang, Y. Zhang, Z. Xiong, G. Yao, B. Lai, An old story with new insight into the structural transformation and radical production of micron-scale zero-valent iron on successive reactivities, *Chin. Chem. Lett.* 31 (2020) 2634–2640.
- [38] X. He, M. Wu, Z. Ao, B. Lai, Y. Zhou, T. An, S. Wang, Metal-organic frameworks derived C/TiO<sub>2</sub> for visible light photocatalysis: simple synthesis and contribution of carbon species, *J. Hazard. Mater.* 403 (2021), 124048.
- [39] M. Xu, Y. Chen, J. Qin, Y. Feng, W. Li, W. Chen, J. Zhu, H. Li, Z. Bian, Unveiling the role of defects on oxygen activation and photodegradation of organic pollutants, *Environ. Sci. Technol.* 52 (2018) 13879–13886.
- [40] C. Cheng, S. Gao, J. Zhu, G. Wang, L. Wang, X. Xia, Enhanced performance of LaFeO<sub>3</sub> perovskite for peroxymonosulfate activation through strontium doping towards 2,4-D degradation, *Chem. Eng. J.* 384 (2020), 123377.
- [41] Y. Zhang, Z. Zhao, J. Chen, L. Cheng, J. Chang, W. Sheng, C. Hu, S. Cao, C-doped hollow TiO<sub>2</sub> spheres: in situ synthesis, controlled shell thickness, and superior visible-light photocatalytic activity (vol 165, pg 715, 2015), *Appl. Catal. B Environ.* 166 (2015), 644–644.
- [42] J. Pan, Z. Dong, B. Wang, Z. Jiang, C. Zhao, J. Wang, C. Song, Y. Zheng, C. Li, The enhancement of photocatalytic hydrogen production via Ti<sup>3+</sup> self-doping black TiO<sub>2</sub>/g-C<sub>3</sub>N<sub>4</sub> hollow core-shell nano-heterojunction, *Appl. Catal. B Environ.* 242 (2019) 92–99.
- [43] S. Ghoreishian, K. Ranjith, H. Lee, H. Ju, S. Nikoo, Y. Han, Y. Huh, Hierarchical N-doped TiO<sub>2</sub>@Bi<sub>2</sub>WxMo<sub>1-x</sub>O<sub>6</sub> core-shell nanofibers for boosting visible-light-driven photocatalytic and photoelectrochemical activities, *J. Hazard. Mater.* 391 (2020), 122249.
- [44] Y. Zhao, B. Huang, H. An, G. Dong, J. Ma, Enhanced activation of peroxymonosulfate by Sr-doped LaFeO<sub>3</sub> perovskite for Orange I degradation in the water, *Sep. Purif. Technol.* 256 (2021), 117838.
- [45] L. Lai, H. Ji, H. Zhang, R. Liu, B. Lai, Activation of peroxydisulfate by V-Fe concentrate ore for enhanced degradation of carbamazepine: surface  $\text{V}(\text{III})$  and  $\text{V}(\text{IV})$  as electron donors promoted the regeneration of  $\text{Fe}(\text{II})$ , *Appl. Catal. B Environ.* (2021) 119559.
- [46] Z. Wu, Y. Wang, Z. Xiong, Z. Ao, S. Pu, G. Yao, B. Lai, Core-shell magnetic Fe<sub>3</sub>O<sub>4</sub>@Zn/Co-ZIFs to activate peroxymonosulfate for highly efficient degradation of carbamazepine, *Appl. Catal. B Environ.* 277 (2020), 119136.
- [47] Z. Shen, H. Zhou, Z. Pan, Y. Guo, Y. Yuan, G. Yao, B. Lai, Degradation of atrazine by Bi<sub>2</sub>MoO<sub>6</sub> activated peroxymonosulfate under visible light irradiation, *J. Hazard. Mater.* 400 (2020), 123187.
- [48] D. Huang, G. Zhang, J. Yi, M. Cheng, S. Chen, Progress and challenges of metal-organic frameworks-based materials for SR-AOPs applications in water treatment, *Chemosphere* 263 (2020), 127672.
- [49] J. Li, M.J. Xu, G. Yao, B. Lai, Enhancement of the degradation of atrazine through CoFe2O4 activated peroxymonosulfate (PMS) process: kinetic, degradation intermediates, and toxicity evaluation, *Chem. Eng. J.* 348 (2018) 1012–1024.
- [50] D. Awfa, M. Ateia, M. Fujii, M.S. Johnson, C. Yoshimura, Photodegradation of pharmaceuticals and personal care products in water treatment using carbonaceous-TiO<sub>2</sub> composites: a critical review of recent literature, *Water Res.* 142 (2018) 26–45.
- [51] Y. Wu, L. Bu, X. Duan, S. Zhu, M. Kong, N. Zhu, S. Zhou, Mini review on the roles of nitrate/nitrite in advanced oxidation processes: radicals transformation and products formation, *J. Clean. Prod.* 273 (2020), 123065.
- [52] J. Wang, S. Wang, Reactive species in advanced oxidation processes: formation, identification and reaction mechanism, *Chem. Eng. J.* 401 (2020), 126158.
- [53] A. Boutiti, R. Zouaghi, S.E. Bendjabeur, S. Guittonneau, T. Schili, Photodegradation of 1-hexyl-3-methylimidazolium by UV/H<sub>2</sub>O<sub>2</sub> and UV/TiO<sub>2</sub>: influence of pH and chloride, *J. Photochem. Photobiol. A Chem.* 336 (2017) 164–169.
- [54] J. Yang, B. Yuan, H. Cui, S. Wang, M. Fu, Modulating oxone-MnO<sub>x</sub>/silica catalytic systems toward ibuprofen degradation: insights into system effects, reaction kinetics and mechanisms, *Appl. Catal. B Environ.* 205 (2017) 327–339.
- [55] S. Li, J.Y. Hu, Photolytic and photocatalytic degradation of tetracycline: effect of humic acid on degradation kinetics and mechanisms, *J. Hazard. Mater.* 318 (2016) 134–144.
- [56] J. Jia, D. Liu, J. Tian, W. Wang, J. Ni, X. Wang, Visible-light-excited humic acid for peroxymonosulfate activation to degrade bisphenol A, *Chem. Eng. J.* 400 (2020), 125853.
- [57] J. Peng, X. Lu, X. Jiang, Y. Zhang, Q. Chen, B. Lai, G. Yao, Degradation of atrazine by persulfate activation with copper sulfide (CuS): kinetics study, degradation pathways and mechanism, *Chem. Eng. J.* 354 (2018) 740–752.
- [58] L. Chen, Y. Zhang, C. Ma, Perovskites Sr<sub>x</sub>La<sub>1-x</sub>Mn<sub>y</sub>Co<sub>1-y</sub>O<sub>3-δ</sub> coated on Ti as stable non-noble anode for efficient electrocatalytic oxidation of organic wastewater containing ammonia nitrogen, *Chem. Eng. J.* 393.
- [59] Z. Xiong, Y. Jiang, Z. Wu, G. Yao, B. Lai, Synthesis strategies and emerging mechanisms of metal-organic frameworks for sulfate radical-based advanced oxidation process: a review, *Chem. Eng. J.* (2020), 127863.
- [60] J. Wang, X. Duan, J. Gao, Y. Shen, X. Feng, Z. Yu, X. Tan, S. Liu, S. Wang, Roles of structure defect, oxygen groups and heteroatom doping on carbon in nonradical oxidation of water contaminants, *Water Res.* 185 (2020), 116244.
- [61] A. Jawad, K. Zhan, H. Wang, A. Shahzad, Z. Chen, Tuning of persulfate activation from radical to non-radical pathway through the incorporation of non-redox magnesium oxide, *Environ. Sci. Technol.* 54 (2020) 2476–2488.
- [62] C. Aggelopoulos, D. Tataraki, G. Rassias, Degradation of atrazine in soil by dielectric barrier discharge plasma – potential singlet oxygen mediation, *Chem. Eng. J.* 347 (2018) 682–694.
- [63] J. Yang, M. Zhu, D.D. Dionysiou, What is the role of light in persulfate-based advanced oxidation for water treatment? *Water Res.* 189 (2020), 116627.
- [64] Y. Zhou, J. Jiang, Y. Gao, J. Ma, S.Y. Pang, J. Li, X.T. Lu, L.P. Yuan, Activation of peroxymonosulfate by benzoquinone: a novel nonradical oxidation process, *Environ. Sci. Technol.* 49 (2015) 12941–12950.
- [65] P. Gao, X. Tian, Y. Nie, C. Yang, Z. Zhou, Y. Wang, Promoted peroxymonosulfate activation into singlet oxygen over perovskite for ofloxacin degradation by controlling the oxygen defect concentration, *Chem. Eng. J.* 359 (2019) 828–839.
- [66] Y. Wang, L. Chen, H. Cao, Z. Chi, C. Chen, X. Duan, Y. Xie, F. Qi, W. Song, J. Liu, S. Wang, Role of oxygen vacancies and Mn sites in hierarchical Mn<sub>2</sub>O<sub>3</sub>/LaMnO<sub>3</sub>-delta perovskite composites for aqueous organic pollutants decontamination, *Appl. Catal. B Environ.* 245 (2019) 546–554.
- [67] A. Fmm, A. Esi, B. Az, A. Ab, A. Mnl, Synthesis of binder-free fluffy anemone-like MoS<sub>2</sub> for electrocatalytic hydrogen evolution: a Mott-schottky study, *Int. J. Hydron. Energy* 45 (2020) 28696–28705.
- [68] D. Zhu, Q. Zhou, Nitrogen doped g-C<sub>3</sub>N<sub>4</sub> with the extremely narrow band gap for excellent photocatalytic activities under visible light, *Appl. Catal. B Environ.* 281 (2020), 119474.
- [69] Z. Zhang, J.T. Yates, Band bending in semiconductors: chemical and physical consequences at surfaces and interfaces, *Chem. Rev.* 112 (2012) 5520–5551.
- [70] S. Guan, H. Yang, X. Sun, T. Xian, Preparation and promising application of novel LaFeO<sub>3</sub>/BiOBr heterojunction photocatalysts for photocatalytic and photo-Fenton removal of dyes, *Opt. Mater.* 100 (2020), 109644.
- [71] D. Kim, K. Yong, Boron doping induced charge transfer switching of a C<sub>3</sub>N<sub>4</sub>/ZnO photocatalyst from Z-scheme to type II to enhance photocatalytic hydrogen production, *Appl. Catal. B Environ.* 282 (2020), 119538.
- [72] Y. Wang, J. Le Roux, T. Zhang, J.P. Croue, Formation of brominated disinfection byproducts from natural organic matter isolates and model compounds in a sulfate radical-based oxidation process, *Environ. Sci. Technol.* 48 (2014) 14534–14542.
- [73] E. Yun, H. Yoo, H. Bae, H. Kim, J. Lee, Exploring the role of persulfate in the activation process: radical precursor versus electron acceptor, *Environ. Sci. Technol.* 51 (2017) 10090–10099.
- [74] L. Lai, H. Zhou, H. Zhang, Z. Ao, Z. Pan, Q. Chen, Z. Xiong, G. Yao, B. Lai, Activation of peroxydisulfate by natural titanomagnetite for atrazine removal via free radicals and high-valent iron-oxo species, *Chem. Eng. J.* 387 (2020), 124165.
- [75] Y. Rao, Y. Zhang, F. Han, H. Guo, Y. Huang, R. Li, F. Qi, J. Ma, Heterogeneous activation of peroxymonosulfate by LaFeO<sub>3</sub> for diclofenac degradation: DFT-assisted mechanistic study and degradation pathways, *Chem. Eng. J.* 352 (2018) 601–611.
- [76] M. Zhang, Y. Gong, X. Zhao, Promoted photoelectrocatalytic degradation of BPA with peroxymonosulfate on a MnFe<sub>2</sub>O<sub>4</sub> modified carbon paper cathode, *Chem. Eng. J.* 399 (2020), 125088.
- [77] M. Tian, M. Ma, B. Xu, C. Chen, C. He, Z. Hao, R. Albilal, Catalytic removal of 1,2-dichloroethane over LaSrMnCoO<sub>6</sub>/H-ZSM-5 composite: insights into synergistic

- effect and pollutant-destruction mechanism, *Catal. Sci. Technol.* 8 (2018) 4503–4514.
- [78] Y. Wang, L. Chen, H. Cao, Z. Chi, S. Wang, Role of oxygen vacancies and Mn sites in hierarchical Mn<sub>2</sub>O<sub>3</sub>/LaMnO<sub>3</sub>-δ perovskite composites for aqueous organic pollutants decontamination, *Appl. Catal. B Environ.* 245 (2019) 546–554.
- [79] G. Wang, C. Cheng, J. Zhu, L. Wang, S. Gao, X. Xia, Enhanced degradation of atrazine by nanoscale LaFe<sub>1-x</sub>Cu<sub>x</sub>O<sub>3</sub>-delta perovskite activated peroxymonosulfate: performance and mechanism, *Sci. Total Environ.* 673 (2019) 565–575.
- [80] C. Dong, Z. Zheng, M. Badsha, J. He, I. Lo, Visible-light-driven peroxymonosulfate activation in photo-electrocatalytic system using hollow-structured Pt@CeO<sub>2</sub>@MoS<sub>2</sub> photoanode for the degradation of pharmaceuticals and personal care products, *Environ. Int.* 154 (2021), 106572.
- [81] J. Li, Y.J. Wan, Y.J. Li, G. Yao, B. Lai, Surface Fe(III)/Fe(II) cycle promoted the degradation of atrazine by peroxymonosulfate activation in the presence of hydroxylamine, *Appl. Catal. B Environ.* 256 (2019), 117782.
- [82] Y. Ji, C. Dong, D. Kong, J. Lu, Q. Zhou, Heat-activated persulfate oxidation of atrazine: implications for remediation of groundwater contaminated by herbicides, *Chem. Eng. J.* 263 (2015) 45–54.
- [83] X. Zhao, C.X. Zhang, S.G. Wang, C. Song, X. Li, Theoretical and experimental study on the degradation mechanism of atrazine in Fenton oxidation treatment, *RSC Adv.* 7 (2017) 1581–1587.
- [84] X. Yao, X. Hu, W. Zhang, X. Gong, X. Wang, S. Pillai, D. Dionysiou, D. Wang, Mie resonance in hollow nanoshells of ternary TiO<sub>2</sub>-Au-CdS and enhanced photocatalytic hydrogen evolution, *Appl. Catal. B Environ.* 276 (2020), 119153.
- [85] J. Zhuang, Q. Tian, H. Zhou, Q. Liu, P. Liu, H. Zhong, Hierarchical porous TiO<sub>2</sub>@C hollow microspheres: one-pot synthesis and enhanced visible-light photocatalysis, *J. Mater. Chem.* 22 (2012) 7036–7042.